Atmospheric Turbulence Simulation Using
Liquid Crystal Spatial Light Modulators

THESIS

James D Phillips, Captain, USAF

AFIT/GEO/ENG/05-01

DEPARTMENT OF THE AIR FORCE
AIR UNIVERSITY

AIR FORCE INSTITUTE OF TECHNOLOGY

Wright-Patterson Air Force Base, Ohio

AFIT/GEO/ENG/05-01

Atmospheric Turbulence Simulation Using Liquid Crystal Spatial Light Modulators

THESIS

Presented to the Faculty

Department of Electrical and Computer Engineering

Graduate School of Engineering and Management

Air Force Institute of Technology

Air University

Air Education and Training Command

In Partial Fulfillment of the Requirements for the

Degree of Master of Science in Electrical Engineering

James D Phillips, B.S.E.E.

Captain, USAF

March 2005

AFIT/GEO/ENG/05-01

Atmospheric Turbulence Simulation Using Liquid Crystal Spatial Light Modulators

James D Phillips, B.S.E.E.

Captain, USAF

Approved:

/signed/	21 Mar 2005
Maj Matthew E. Goda, PhD Thesis Advisor	date
/signed/	21 Mar 2005
Dr. Won B. Roh Committee Member	date
/signed/	21 Mar 2005
Dr. Stephen Cain Committee Member	date
/signed/	21 Mar 2005
Dr. Troy Rhoadarmer Committee Member	date

AFIT/GEO/ENG/05-01

Abstract

Laser systems are finding a home in many military applications - such as Space Situational Awareness, imaging and weapons systems. With an increasing focus on programs that entail atmospheric propagations, there is a need for a cost effective method of performing laboratory proof-of-concept demonstrations. The use of one SLM (single phase screen) to model atmospheric effects has been investigated previously with promising results. However, some effects cannot be captured with a single SLM. This paper focuses on the addition of a second SLM and quantifying the results. Multiple screens will allow the user to independently control the Fried parameter, the isoplanatic angle, and Rytov Variance.

The research is comprised of simulation and experiment. The simulation demonstrates the ability to accurately model atmospheric effects with two phase screens. Based on the simulation, a hardware implementation was tested in the lab. The results of this research show promise, however some issues remain. This thesis describes the experimental set-up and results based on measurement of phase and intensity of the propagated field. It was noted that while analytic results are replicated in simulation, similar results in the lab were difficult to achieve. The combined diffractive effect of two small apertures (SLMs) is thought to be a predominant error source.

Acknowledgements

Table of Contents

List of Figures

x

List of Tables

Atmospheric Turbulence Simulation Using Liquid Crystal Spatial Light Modulators

I. Introduction

1.1 Research Motivation

Laser systems are finding a home in many military applications; these applications include Space Situational Awareness (SSA), imaging and weapons systems. These systems often require a laser beam to be propagated through the atmosphere. Naturally occurring temperature changes and wind currents cause the atmosphere to have a spatially and temporally varying index of refraction. This randomly varying index causes beam aberrations such as beam spreading, beam wander, and scintillation. With an ever increasing focus on Space Situational Awareness (SSA) and other optical programs that require atmospheric propagations, there is a need for an efficient method of performing proof of concept demonstrations in the presence of these types of aberrations.

Few options exist for bench testing optical systems in the presence of turbulence. The methods that do exist for simulating turbulence include vibrating of thin reflective membranes, and phase wheels. The reflective membranes and phase wheels are less than ideal in that they cannot be dynamically changed; every atmospheric test condition would require optical adjustment or a new set of phase wheels. It is desirable to have a bench top system that can be computer controlled to allow for rapidly reconfigurable testing in different turbulence environments. The use of Liquid Crystal (LC) Spatial Light Modulators (SLM) shows promise to be able to provide this capability.

The use of one SLM phase screen to simulate atmospheric turbulence has been investigated previously with promising results [4]. The interest in adding multiple phase screens results from propagation through extended turbulence. As these beams

propagate the spatial extent of the beam is changed and therefore the properties of the turbulence experienced also changes. By adding multiple phase screens spaced over the propagation distance we can begin to account for this effect. Also when using a natural guide star in imaging, it is crucial to accurately model anisoplanatic effects, which is not possible with a single screen.

Multiple screens will allow the user to simultaneously control r_0 (a parameter representing turbulence strength), θ_0 (the isoplanatic angle), and σ_1^2 (a parameter linked to the intensity distribution of a plane wave). With a single screen r_0 is determined by the strength of the screen and is independent of screen location; the other parameters are dependent on screen location and cannot be independently controlled in a single screen model. By creating a two or three screen model you gain the ability to control each of the parameters independent of the others; also you can vary θ_0 and σ_1^2 without physically moving the screens.

A bench top system to create atmospheric turbulence conditions would allow for much more cost efficient and rapid testing. The cost savings would be realized in the ability to eliminate bad ideas prior to going to the field to test and to debug good systems more fully in the lab. Critical parameters could be isolated allowing for faster resolution to noted problems. This would also allow the system to be optimized prior to field testing. Testing could be performed much more rapidly because it would not be necessary to wait on required test conditions or risk being weathered out.

Other benefits include being able to test competing ideas in identical turbulence scenarios; this makes it much easier to rapidly select the best system to pursue. Also a controllable lab system would allow testing in extreme turbulence conditions which may not occur at field test sites. This would enable the testing of systems to the very limit of the specifications.

If SLMs prove to effectively add aberrations to an optical field, they may also be useful to simulate adaptive optical elements, such as deformable mirrors, in a lab setting.

1.2   Problem Description

This document focuses on the design and implementation of a bench top system to induce optical aberrations onto wavefronts using multiple liquid crystal (LC) spatial light modulators (SLM). Simulation and analysis will be done to determine how well key atmospheric parameters can be controlled using a two or three phase screen model. Simulation and analysis will also be done to determine the effects of diffraction that results from the fill factor of the SLMs. The results of simulation will then be verified by bench testing.

1.3   Research Objectives

1. Further previous research [4] by demonstrating that higher fidelity turbulence models for long atmospheric propagations can be implemented using multiple SLMs.

2. Characterize the behavior of the chosen SLMs. Attention should be paid to the diffraction and fill factor effects.

3. Demonstrate two screen models give acceptable control over three atmospheric parameters: r_0, θ_0, and σ_1.

4. Validate the lab results through comparison to accepted models.

1.4   Methodology

In the atmosphere, laser device effectiveness degrades due to beam spread and distortion caused by propagation through random nonuniform media. In particular, the wavefront of the E-field describing light is manipulated by variations of refractive index in the media. A system that can mimic refractive index variations in the atmosphere can produce similar distortion effects on laser light that the atmosphere would produce. A spatial light modulator (SLM) is used to implement this concept. The SLM is composed of an array of pixels where each pixel has a controllable index of refraction. Changing these individual pixel indices allows the wavefront passing

through the device to be altered as specified by the user. Therefore, it is possible to generate atmospheric phase screens (representations of how the atmosphere changes wavefronts) to imprint on the SLM and aberrate wavefronts in a fashion similar to the atmosphere.

To produce phase screens, the atmosphere is modeled using well established theory and data on refractive index variations. Random statistics of these variations can be captured using the structure function, which describes the randomness of the atmosphere. Using the structure function, the power spectrum describing the frequency content of index variations can be found [1]. Finally, the power spectrum leads to the desired phase screens by using a Fourier series technique. The structure function, power spectral density, and phase screen generation topics will all be defined and discussed in Chapter 2. Resultant phase screens can then be loaded to the SLMs so that the phase of the wavefront is manipulated to represent the atmosphere. In this way, atmospheric effects on optical systems can be reproduced in the lab. This thesis consists of a lab experiment and computer simulation of the system.

1.4.1 Experimentation. An optic test is performed in the lab to show that SLMs are a viable substitute for the real-world atmosphere in testing laser and imaging devices. When implemented, the aberrating system consists of a laser source emitting light onto an SLM that reflects light toward a second SLM; the light is then reflected into two sensors to measure the SLMs' modification to the laser light. For the source, a helium-neon laser with 3mW output power is used. Passing the HeNe beam through a spatial filter approximates a point source which is collimated using a lens. Collimating the beam allows benchmark testing and facilitates system verification. To ascertain the effects of the system, a targetboard CCD array, and Shack-Hartmann wavefront sensor are used. To control the aberrating system, a computer interface is used that requires 0 - 255 gray level images to communicate the phase modulation to the SLMs. Phase screens mimicking the atmosphere can be loaded to the SLMs in the gray level format. In order to transcribe generated phase screens to the SLMs so that light

behaves in the desired manner, the phase screen pixel values must be modified based on the characteristics of the SLM. These characteristics include diffraction due to the geometry of the system and a nonlinear phase delay behavior that influence the wavefront's behavior in undesirable ways.

1.4.2 Computer Simulation. Alongside the lab experiment computer simulations are performed. In addition to verifying system behavior, simulation also allows the user to explore and isolate the undesirable effects caused by the SLM. The simulations are accomplished using Wavetrain, an available wave optics propagation code. Diffraction effects were isolated and modeled in Matlab; this was done due to the impact diffraction has on the final results.

1.5 Implications

This research demonstrates the ability of an SLM to introduce specified aberrations into an optical system for laser light. With the ability for the user to control exactly what aberrations are present in the system, it is possible to evaluate system performance under the usual and unusual conditions of use. The SLM device is of most use when testing optic that would operate in the Earth's atmosphere. Using atmospheric models in conjunction with phase screen generation to simulate atmospheric aberrations means completing lab tests where field testing was once required. A tool that accepts input of any known atmospheric model or data will enable a wide range of atmospheric behaviors as well. Optical designs can be evaluated in-lab with simulated atmospheric conditions so that design improvements can be more quickly implemented. Air Force research involving laser systems will benefit from a tool that simulates atmospheric conditions in a lab environment. Specifically, design and evaluation times should be significantly reduced.

1.6 Summary

Evaluating optical systems for laser devices can be a cumbersome task in the development process because of the amount of time needed for the complexities and logistics of field testing. Recreating real world optical conditions in the lab using a liquid crystal spatial light modulator allows realistic and controllable atmospheric aberrations to be inserted into an optic system so that testing time is shortened. Producing atmospheric aberrations is done by modeling the atmosphere and generating phase screens for use on SLMs. These phase screens are produced by using Fourier series implementation of the power spectrum describing index of refraction variations. The SLM is then characterized so that abnormalities altering phase screen behavior can be compensated. These abnormalities include a nonlinear phase relationship to gray levels and diffraction due to a fill factor of 83% causing light to be diffracted in multiple directions off the optic axis. Correcting these issues allows for a controllable device to simulate many types of atmospheric conditions.

II. Theory

The purpose of this study is to determine if a system can be created to simulate propagation of laser light through a turbulent atmosphere. In order to understand the problem some basic theory must be understood. The following sections present a brief discussion of diffraction, atmospheric turbulence theory, and phase screen generation.

2.1 Light Propagation and Diffraction

To properly understand how light propagates through various media one must understand reflection, refraction, and diffraction. For purposes of this thesis all are important but diffraction will play a dominant role.

Diffraction is defined by Sommerfeld as any deviation of light from rectilinear paths which cannot be interpreted as reflection or refraction. Diffraction is caused by the confinement of the lateral extent of the wavefront and is most noticeable with confinement sizes on the order of a wavelength.

2.1.1 History.

The first description of such a phenomenon was by Grimaldi and was published in 1665. He used a small light source to illuminate an aperture and observed the intensity on an observing screen. The pattern he saw had soft edges that were contrary to the corpuscular theory of light. In 1678, Christian Huygens introduced his theory of secondary wavelets. This theory stated that any propagating wavefront can be modelled a series of new sources of spherical disturbances and the new wavefront is the envelope of these secondary wavefronts.

In the early 1700s Thomas Young introduced the idea of interference, which states that under proper conditions light can be added to light to produce dark.

Augustin Jean Fresnel brought together the work of Huygens and Young. By making some assumptions about the amplitude and phase of Huygens' secondary wavelets and allowing them to mutually interfere he was able to predict light distributions very accurately. In 1882 Gustav Kirchoff gave more credibility to Fresnel's

work by showing that his assumptions were a natural result of the wave nature of light described by Maxwell. Due to some inconsistencies in Kirchoff's mathematical formulation, the Huygens-Fresnel principle must be regarded as an approximation–although under most conditions a very accurate one. Later work by Sommerfeld eliminated Kirchoff's inconsistant assumptions and led to the Rayleigh-Sommerfeld diffraction integral, which forms the basis of the Huygens-Fresnel principle [8]. The Huygens-Fresnel integral will be used as the starting point for the theory development in this thesis.

$$U(x,y) = \frac{z}{j\lambda} \int\int_{\Sigma} U(\xi,\eta) \frac{e^{jkr}}{r^2} dS \tag{2.1}$$

where

$$r = \sqrt{(x-\xi)^2 + (y-\eta)^2 + z^2} \tag{2.2}$$

2.1.2 Fresnel Propagation. The only restriction in equation 2.1 is $\sqrt{(x-\xi)^2 + (y-\eta)^2 + z^2} \gg \lambda$; we can make a more usable expression with little loss of accuracy by adding certain approximations. Using the binomial expansion of the square root given by

$$\sqrt{1+b} = 1 + \frac{1}{2}b - \frac{1}{8}b^2 + ... \tag{2.3}$$

we can rewrite r from equation 2.2

$$r \approx z[1 + \frac{1}{2}(\frac{x-\xi}{z})^2 + \frac{1}{2}(\frac{y-\eta}{z})^2] \tag{2.4}$$

By taking the full form of equation 2.4 in the exponential term and only the first term in the denominator term equation 2.1 simplifies to

$$U(x,y) = \frac{e^{jkz}}{j\lambda z} \int\int_{\Sigma} U(\xi,\eta) e^{\frac{jk}{2z}[(x-\xi)^2+(y-\eta)^2]} d\xi d\eta \tag{2.5}$$

8

By expanding the quadratic terms in the exponential and applying the definition of the Fourier transform this equation can be rewritten as

$$U(x,y) = \frac{e^{jkz}}{j\lambda z} e^{\frac{jk}{\lambda z}(x^2+y^2)} \mathcal{F}[U(\xi,\eta)e^{\frac{jk}{2z}(\xi^2+\eta^2)}] \tag{2.6}$$

evaluated at $f_x = \frac{x}{\lambda z}$ and $f_y = \frac{y}{\lambda z}$. This final form of the Fresnel integral will form the basis for all simulations and analysis in this thesis.

In Matlab, the Fresnel propagation is performed using a two dimensional Fast Fourier Transform (FFT) algorithm; the problem with this approach is that it does not allow the user to select the grid spacing in the output array. This can be alleviated by doing a two step Fresnel propagation; first propagating to an intermediate plane and then to the output plane. By proper selection of the intermediate plane location the user can precisely control the output array size [10]. The intermediate plane location is selected according to

$$z_{intermediate} = z_{total}(\frac{\Delta\rho}{\Delta r + \Delta\rho}) \tag{2.7}$$

where $z_{intermediate}$ is the location of the intermediate plane, z_{total} is the total propagation distance, $\Delta\rho$ and Δr are the extent of the field to be sampled in the input and output planes, respectively.

Whenever a given field is input to a digital simulation, accuracy of results greatly depend on the sample spacing and wavefront extent. A field that is insufficiently sampled to represent the highest frequency components in both amplitude and phase produces erroneous results. Therefore care must also be taken in selecting the input and output sample sizes to satisfy sampling requirements. It is necessary to chose spacings small enough that the wavefront is properly sampled but large enough to capture the region of interest and avoid wrap-around effects [5]. If the input and output sample sizes are chosen to be equal, the sampling requirement is satisfied by

$$\delta = \frac{\lambda z_{total}}{2D} \tag{2.8}$$

where δ is the sample size, and D is the extent of the field to be sampled.

2.2 Atmospheric Turbulence Theory

The above propagation theory applies to light propagation in a medium with uniform index of refraction. In the atmosphere this is clearly not the case. The consequence of this is that atmospheric turbulence becomes the limiting factor for resolution for most optical systems that require a long propagation through the atmosphere. In long exposure imaging, the point spread function (PSF) of the imaging system is very broad and smooth; while in short exposure imaging, known as speckle imaging, the PSF is not quite as broad but suffers from a modulated (speckled) irradiance pattern. In either of these two cases angular resolution is severely limited [11].

Turbulence effects result from random spatial and temporal fluctuations in index of refraction in the atmosphere, which in turn cause a random variation in optical path length (OPL). These variations in OPL result in phase abberations on the wavefront, which in turn become intensity variations after the wave has propagated. Turbulence is a stochastic process and therefore it is not tractable to model as a deterministic process. Since atmospheric turbulence is not easily modeled as a deterministic process, statistical models are required to understand and model these effects. This first of these models was created in the 1940's by A.N. Kolmogorov.

The atmosphere can be considered a viscous fluid, and therefore it has two distinct states of motion - laminar and turbulent. The distinction between these two states is that laminar flow is smooth and regular while turbulent flow is unstable and acquires random subflows called turbulent eddies. The separation between these two regimes is defined by the Reynolds number:

$$Re = \frac{v_{avg}l}{k_v} \tag{2.9}$$

10

When the Reynolds number exceeds some critical value the flow is said to be turbulent. The viscosity of air is $k_v = 1.5 \times 10^{-5} \frac{m^2}{s}$, and assuming a scale size of $l = 10m$ and a velocity of $v_{avg} = 1\frac{m}{s}$, a Reynolds number of 6.7×10^5 is found. This example demonstrates that atmospheric air flow is essentially always turbulent [11].

In Kolmogorov's theory he suggested that the structure of the atmosphere, for large Reynolds numbers, was homogenous and isotropic within the inertial subrange. Inside the inertial subrange the atmosphere is comprised of eddies that interact and exchange energy to form and divide into smaller eddies. An eddy is defined as a pocket of air that has a uniform temperature and pressure. The inertial subrange is defined by eddy sizes bounded by the inner scale, l_0, and the outer scale, L_0.

Index of refraction variations in the atmosphere result from temperature inhomogeneities caused by turbulent air motion. Since temperature fluctuations are a function of location in space, $\mathbf{R}$, and time, t, so is the index of refraction:

$$n(\mathbf{R}, t) = n_0 + n_1(\mathbf{R}, t), \tag{2.10}$$

where $n_0 \approx 1$ is the mean value of the index of refraction and $n_1(\mathbf{R}, t)$ is the deviation about this mean. The index of refraction time dependence can be ignored since the rate of change of the atmosphere is slow when compared to the typical timescales of turbulence moving across the beam (Taylors Frozen Flow). Using these simplifications, the index of refraction can be represented by

$$n(\mathbf{R}) = 1 + n_1(\mathbf{R}), \tag{2.11}$$

Using equation 2.11, it is possible to arrive at the structure function describing the index of refraction variations in the atmosphere.

The structure function is necessary because it is not possible to exactly describe the index of refraction random process for all positions in space. There are too many random behaviors and variables to account for in a closed form solution. The index

11

can only be described in reference to stationary random functions. Over long spatial periods, the index of refraction is not a stationary random process, but over short spatial periods of interest to applications of laser propagation, the index is considered to have stationary increments [1]. In other words, it is possible to treat the index random process as stationary with emphasis on the function $n(\mathbf{R} + \mathbf{R_1}) - n(\mathbf{R_1})$. Intuitively, the structure function of the index of refraction is the mean squared difference between the index of refraction at one point in space and the index at a point with some separation distance from the first point. The structure function of $n(R)$ is defined by:

$$D_n(\mathbf{R_1}, \mathbf{R_2}) = \langle [n(\mathbf{R_1}) - n(\mathbf{R_2})]^2 \rangle \tag{2.12}$$

where $\mathbf{R_1}$ and $\mathbf{R_2}$ are vectors describing points in space and $\langle \cdot \rangle$ denotes the ensemble average. By starting with the structure function of wind velocity Kolmogorov was able to determine the structure function of the index of refraction to be:

$$D_n(R) = \begin{cases} C_n^2 R^{2/3} & , \quad l_o \ll R \ll L_o \\ C_n^2 l_o^{-4/3} R^2 & , \qquad R \ll l_o \end{cases} \tag{2.13}$$

where l_0 and L_0 are the inner and outer scale sizes, $R = \mathbf{R_2} - \mathbf{R_1}$, and C_n^2 is the atmospheric structure constant. At small scale sizes below l_o, the structure function follows a squared relationship (second part of Equation 2.13) which is found by performing a Taylor Series expansion on the structure function for small separation distances [1]. The structure function is dependent on the separation distance R and has units of radians squared; it can be written in terms of the atmospheric Fried parameter:

$$D_n(R) = 6.88 \left(\frac{R}{r_o} \right)^{5/3}, \tag{2.14}$$

where r_o relates to turbulence strength and is defined and discussed in a later section.

The structure function is related to the autocorrelation function by:

$$D_n(R) = 2[\Gamma_n(0) - \Gamma_n(R)] \tag{2.15}$$

Further the autocorrelation function, when it exist, is related to the power spectral density (PSD) , $\Phi_n(\kappa)$ by the *Wiener-Khinchin theorem* :

$$\Gamma_n(\mathbf{R}) = \int_{-\infty}^{\infty} \Phi_n(\vec{\kappa}) e^{j\vec{\kappa}\cdot\mathbf{R}} d\vec{\kappa} \tag{2.16}$$

From this relation a spectral model for the atmosphere can be developed.

The statistical distribution of size and number of turbulent eddies is described by the PSD of n, $\Phi_n(\vec{\kappa})$ where $\vec{\kappa}$ is the spatial wavenumber vector. The PSD can be thought of as a measure of the relative abundances of turbulent eddies at a given scale size. Using the assumption that the index of refraction is homogenous and isotropic, the PSD can be written as a function of the scalar wavenumber, κ [11]. Kolmogorov's theory only predicts a form for the PSD inside the inertial subrange:

$$\Phi_n(\kappa, z) = 0.033 C_n^2(z) \kappa^{\frac{-11}{3}} \tag{2.17}$$

where $C_n^2(z)$ is the structure constant of the atmosphere as a function of location in the propagation path, z.

The Kolmogorov spectrum is not valid for all wavenumbers so a more complete model is required. For a more complete model the *modified atmospheric spectrum* will be used and is given by [1]:

$$\Phi_n(\kappa, z) = 0.033 C_n^2(z) \left[1 + 1.802\left(\kappa/\kappa_l\right) - 0.254\left(\kappa/\kappa_l\right)^{7/6} \right] \frac{\exp\left(-\kappa^2/\kappa_l^2\right)}{(\kappa^2+\kappa_o^2)^{11/6}} \quad, \quad 0 \le \kappa \le \infty \tag{2.18}$$

where $\kappa_l = \frac{3.3}{l_o}$ and $\kappa_0 = \frac{1}{L_o}$. This power spectrum is significant in that it is used to generate phase screens representing the atmosphere to load to the SLM. The atmospheric model can be tailored by selecting appropriate inner scale, outer scale, and C_n^2 values depending on the laser beam propagation scenario.

The strength of turbulence in the atmosphere, C_n^2, depends on height above ground (h in meters) and the model chosen. Total turbulence strength for the entire

13
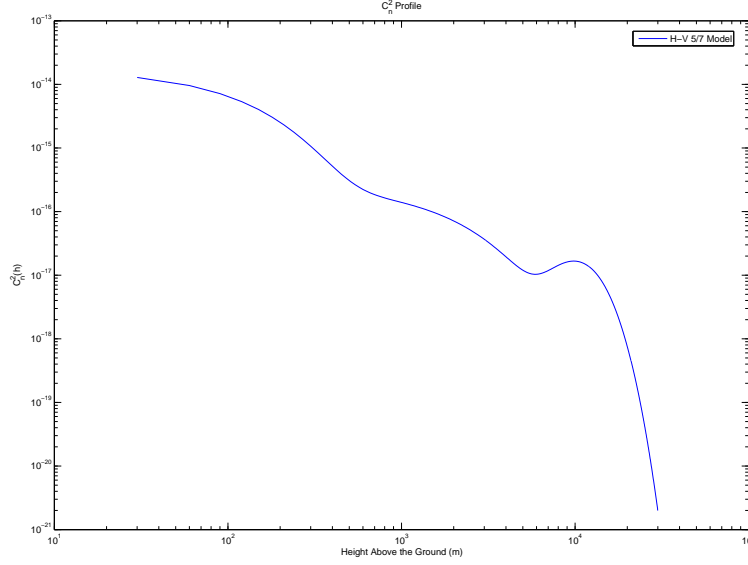
Figure 2.1: C_n^2 Profile example.

path is found by integrating $C_n^2(h)$ over the path that laser light would travel to the sensor. To accomplish this task, the Hufnagel-Valley (H-V) model is chosen describing $C_n^2(h)$. Like the modified spectrum for the atmosphere, the H-V model is most commonly used for generic conditions describing $C_n^2(h)$, as it is based on real data of various seasons, altitudes, and geographic locations [1]. The H-V model used is

$$C_n^2(h) = 0.00594(v/27)^2(10^{-5}h)^{10}\exp(-h/1000) + 2.7\times 10^{-16}\exp(-h/1500)$$
$$+ A\exp(-h/100)$$

$$(2.19)$$

with v as the root-mean-square wind speed in (m/s) and A as the value of $C_n^2(0)$ at the ground in $m^{-2/3}$. An example of an atmospheric profile can be seen in Figure 2.1.

2.2.1 Atmospheric Parameters. Three atmospheric parameters are of interest in this research: the Fried parameter, r_0; the isoplanatic angle, θ_0; and the Rytov variance, σ_1^2. Each of these parameters is a different moment of C_n^2 and is defined

14

below:

$$r_0 = 1.67 \left[k^2 \int_0^L C_n^2(z) dz \right]^{-3/5} \tag{2.20}$$

$$\theta_0 = \left[2.91 k^2 \int_0^L z^{5/3} C_n^2(z) dz \right]^{-3/5} \tag{2.21}$$

$$\sigma_1 = 2.25 k^{7/6} \int_0^L C_n^2(z) z^{5/6} dz \tag{2.22}$$

The Fried parameter defines the roll off of the OTF of the atmosphere [11]; another way of saying this is that little is gained in resolution for aperture sizes larger than r_0. The isoplanatic angle represents the largest field of view over which the optical path length through turbulence does not differ significantly from the on axis path length through turbulence [11]. The Rytov variance is a parameter that describes the irradiance fluctuations associated with an unbounded plane wave [1]. These parameters together give a relatively complete turbulence description.

2.3 *Phase Screens*

For long propagations through a non-uniform media it is necessary to have a way of modeling the phase perturbations as discrete sheets of phase that can be added to the unperturbed wave. This type of model is called a phase screen. Depending on the effects to be modeled and the level of accuracy required one phase screen may or may not be sufficient. If more than one phase screen is used the strength of each screen must be adjusted accordingly. If r_0 is used to define the strength of the atmosphere then each phase screen can be assigned a strength according to

$$r_0^{-5/3} = \sum_{i=1}^N r_{0i}^{-5/3} \tag{2.23}$$

where r_{0i} is the Fried parameter of the individual phase screens [11, 72].

15

2.4 Phase Screen Creation

Modeling the atmosphere using knowledge of the scenario and power spectrum allows phase screens to be produced to represent the atmospheric random process. These phase screens can then be loaded onto the spatial light modulator to affect light in the desired manner. Several methods exist for producing phase screens using the power spectrum. Two common methods involve using the Zernike polynomial basis set to produce phase screens and using the inverse Fourier transform of the power spectrum with Gaussian random variables to produce phase screens. The Fourier transform method is more desirable for this research because of its ability to match a square screen implementation with the square layout of the SLM. One disadvantage in the Fourier transform method is that for simulations over longer time periods, an increasingly large screen must be computed. Additionally, the Fourier transform method produces screens that lack low frequency accuracy. In other words, the modified spectrum to be modeled contains a large percentage of power in the low frequency components. In taking the inverse Fourier transform, these low frequency regions are not allocated enough samples, so low frequencies are under-represented. To alleviate these two problems, a modification to the Fourier transform method is used called the "generalized Fourier series method " [9]. A sample phase screen created using this method can be seen in Figure 2.2.

To facilitate understanding the Fourier series method, the power spectrum must be discussed in relation to random processes. Intuitively, the power spectrum of a random process is the average amount of power in each frequency component composing the random process. For this case, the random process is phase variation induced by the atmosphere. The power spectrum is related to the covariance of the phase variation, $B_n(R)$ by the *Wiener-Khintchine theorem* (recall equation 2.16).

Starting with the modified power spectrum representing the atmosphere (equation 2.18), one can finely sample the PSD the low frequency region and then give fewer samples to the high frequency region. In this way, the frequency regions that
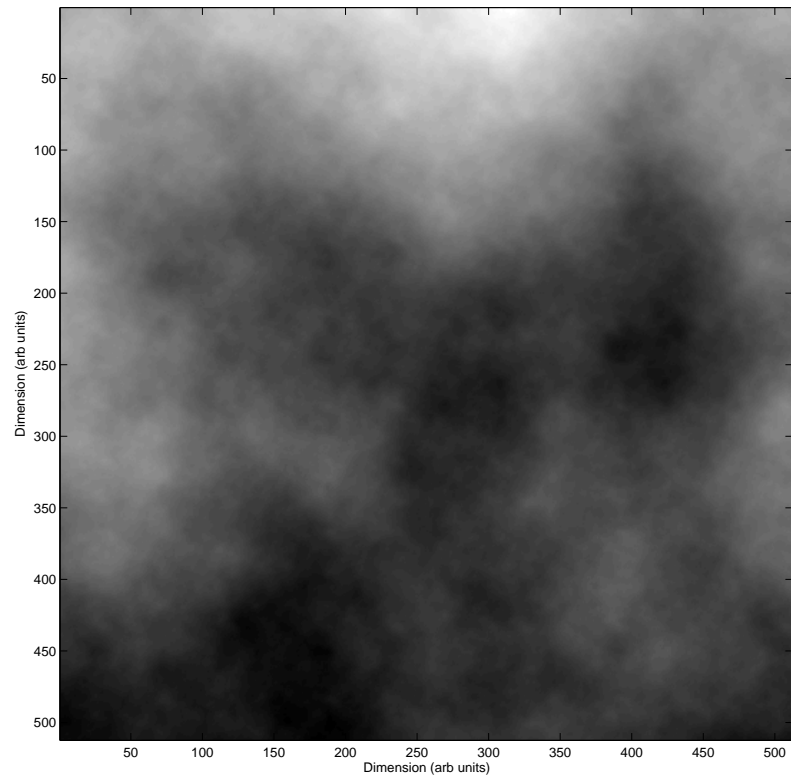
Figure 2.2:   Example Phase Screen Created Using Fourier Series Method.

have a larger power are sampled more often. The PSD is then randomized using Gaussian variables with the appropriate variance. The result is an array of complex coefficients describing the frequency composition of a phase screen iteration. The complex coefficients exhibit circular complex Gaussian statistics with a variance corresponding to the previously sampled PSD. All that remains is to sum sinusoids of corresponding frequencies to produce the desired phase screen. Implementing this procedure is accomplished by the inverse Fourier series given by

$$\phi_k(x, y) = \sum_{n=-\infty}^{\infty} \sum_{m=-\infty}^{\infty} \mathbf{c}_{n,m} e^{j2\pi(f_{x_n}x + f_{y_m}y)}, \qquad (2.24)$$

where (x, y) are spatial coordinates of the screen, $\mathbf{c}_{n,m}$ are randomized complex coefficients from the PSD of interest, and (f_{x_n}, f_{y_m}) are spatial frequency components from the PSD. Note that the sum is calculated rather than using a FFT; this is necessary due to the nonlinear sampling method. By randomizing the real part of the PSD using a circular complex Gaussian random variable, complex coefficients $\mathbf{c}_{n,m}$ are created containing a random phase. Therefore, each phase screen iteration $\phi_k(x, y)$ is unique and possesses a unique random phase in the Fourier domain.

An advantage in this method appears for applications requiring a sequence of screens to represent longer time periods (several seconds). Instead of calculating one large phase screen and moving the area of interest around the screen as time progresses, it is only necessary to calculate the screen exactly where it is needed. Although the generalized Fourier series method cannot take advantage of fast Fourier transform algorithms, calculations are still saved by only calculating the screen area of interest. To implement the Fourier series method, a PSD for the turbulence of interest is calculated using l_0, L_0, r_0 and the spatial frequency region of concern. The Fourier series coefficients are then calculated for frequency components of interest (calculating more low frequency components). Afterward, the coefficients are used to construct the phase screen by summing sinusoids with different weights at any location desired.

18
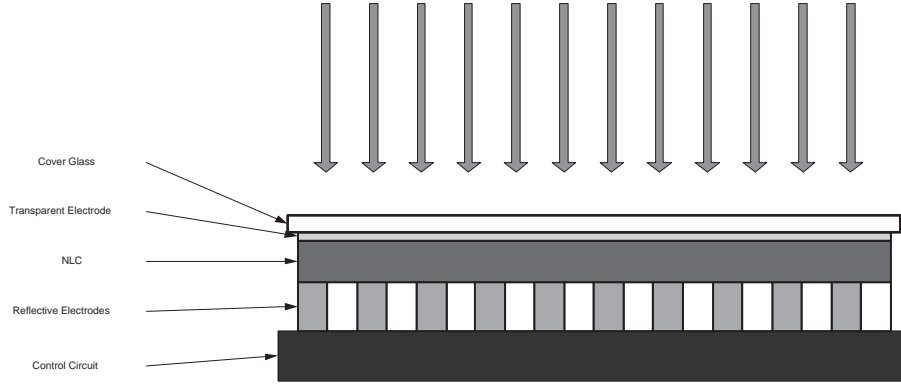
Figure 2.3:   Cross Section of Liquid Crystal Spatial Light Modulator.

2.5   Liquid Crystal Theory

2.5.1   Mechanical Properties of Liquid Crystals.   Liquid Crystal (LC) materials are unique from a physical standpoint because they possess properties of both solids and liquids. The molecules in a LC material are elliptical around a single long axis and possess circular symmetry in the transverse plane. Adjacent molecules are not rigidly bound to one another; they can rotate and slide with respect to one another with the application of an outside stimulus. The outside stimulus can be mechanical or electrical. Although the molecules have the freedom to move somewhat independently there are limits to this movement, giving the material some of the properties of a solid [8].

There are three classes of LC materials: nematic, smectic, and cholesteric. The classes are divided based on the molecular orders or organizational constraints. This research is only interested in nematic LC devices. In a nematic LC device the molecules throughout the device are oriented parallel to one another but the centers are randomly located. In order to give the LC molecules in the SLM a preferred direction the inside surface of the cover glass is covered with score lines; the molecules tend to align themselves with these lines.

The elliptical shape of the LC molecule can be thought of as representing a refractive index ellipse. If the ellipse can be rotated properly we can control the index

19

of refraction seen by the incident light. Birefringent materials are discussed in more detail below.

2.5.2 Birefringent Materials. In a birefringent material the phase velocity, v_p, depends on the polarization and propagation direction of the propagating wave due to a variation in the refractive index with polarization and propagation direction. A birefringent crystal will have two preferred or eigen-polarizations known as the ordinary and the extraordinary waves. The ordinary wave has a constant index of refraction regardless of propagation direction, where the extraordinary wave index is a function of propagation direction. If incident light has a polarization direction that is not exactly parallel to one of these directions the polarization state will change as it propagates through the crystal. If the incident light is polarized in a direction parallel to either of these eigen-polarizations the polarization state will remain unchanged as the wave propagates. This can be shown using Jones Calculus; consider an input field with light polarized along both the fast and the slow axis of a crystal (V_e and V_o are complex field amplitudes aligned in the extraordinary and ordinary directions respectively). The output polarization components can be found by

$$\begin{bmatrix} V_e' \\ V_o' \end{bmatrix} = \begin{bmatrix} \exp(-jn_e \frac{\omega}{c} l) & 0 \\ 0 & \exp(-jn_o \frac{\omega}{c} l) \end{bmatrix} \begin{bmatrix} V_e \\ V_o \end{bmatrix} \qquad (2.25)$$

If $V_o = 0$ then $V_o' = 0$. The matrix in equation 2.25 is a generic matrix used to describe a birefringent material where ω is the frequency of the incident light, l is the thickness of the crystal, and c is the speed of light in vacuum. This is important because if we can orient a crystal such that light is polarized parallel to the extraordinary wave polarization and the crystal can be rotated in a manner to maintain this alignment, we can control the index of refraction seen by the light without causing any change in polarization [12]. In the LC device used for this research the crystal structure is

20
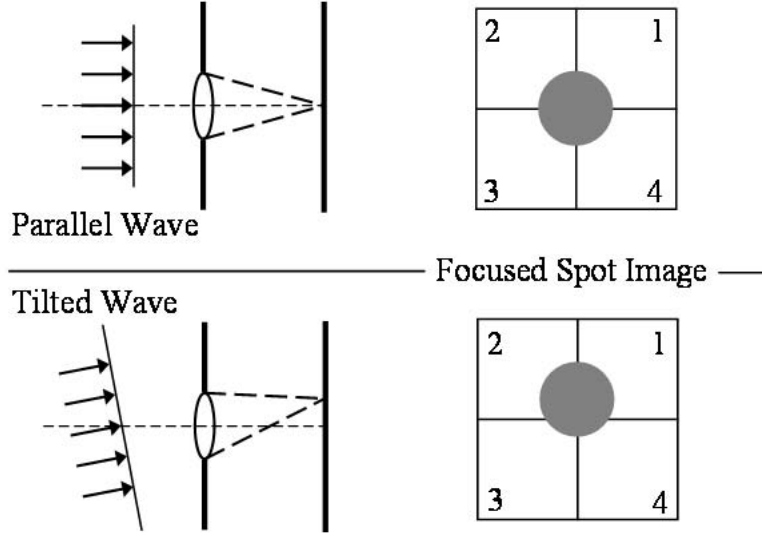
Figure 2.4:   Light incident on a lenslet of the wavefront sensor.

rotated by the application of an **E**-field. The index is controlled according to

$$\frac{1}{n_e^2(\theta)} = \frac{\cos^2(\theta)}{n_o^2} + \frac{\sin^2(\theta)}{n_e^2} \tag{2.26}$$

where n_o and n_e are the ordinary and extraordinary indices, and $n_e(\theta)$ is the effective index seen by an extraordinary ray propagating at an angle, θ, to the optic axis of the crystal. By controlling the index of refraction at each pixel individually, a map of phase delays can be placed onto the SLM. The maximum phase delay in radians that can be experienced by incident light is

$$Delay_{max} = \frac{2\pi(n_e - n_o)l}{\lambda} \tag{2.27}$$

where l is the thickness of the liquid crystal.

2.6   Wavefront Sensing

A Shack-Hartmann wavefront senor is used in this research to measure and verify correct system operation. The wavefront sensor measures the slope of the wavefront

21

of light (the E-field phase) that is reflected from the SLM. It is not possible to directly measure the phase of light in the same way that one would measure the magnitude (actually magnitude squared). Instead, a wavefront sensor treats the incident light as many different samples which are individually analyzed. To understand a wavefront sensor's functionality, consider a simple optical system with an aperture and a lens to focus light at a distance behind the lens as in Figure 2.4. If a plane wave parallel to the aperture fell incident on the system, the intensity pattern observed would be a spot on the optic axis of the system as in the top of Figure 2.4. Similarly, if this same plane wave fell incident on the aperture at an angle (has some tilt), it would produce a spot shifted in some direction proportional to the amount of tilt of the plane wave as in the bottom of Figure 2.4. The focal plane of this system is made up of four intensity detectors arranged in a square, called a quad-cell. Tilt in the x direction can be determined by averaging the left two detectors' intensities and subtracting from the average of the right two detectors' intensities. For y direction tilt, average the top two detectors' intensities subtracted from the bottom two detectors' intensities. Putting several of these systems side-by-side in an array would produce a map of local tilt measurements in the x and y directions. These measurements can then be used to reconstruct the phase that was incident on the wavefront sensor. Reconstructed wavefronts can then be compared to simulated results.

2.7 System Scaling

System scaling is a significant issue because the SLM being used has a height and width of only 7.68 mm. In addition, propagation for a typical indoor lab environment may only be one or two meters. In contrast, many optical systems operating in the atmosphere have an effective diameter of a quarter of a meter or more and propagate over kilometers. To compare optical systems of different sizes, the Fresnel number is often used. The Fresnel number is a parameter that relates wavelength (λ), source aperture radius (a), and propagation distance (L) and is useful to indicate the strength

of diffraction effects due to propagation in an optical system. It is given by:

$$F = \frac{a^2}{\lambda L},\qquad(2.28)$$

A large Fresnel number ($F > 1000$) indicates light propagation in a manner predicted by geometric optics. $F \ll 1$ indicates a strong influence of diffraction on light propagation and a Fourier transform can be used as in Equation 2.6 to calculate a field at a certain distance. When comparing two systems of unequal scale, it is important that the Fresnel number be near identical for each system, so that the effects of diffraction are also nearly equal. In a system with multiple propagation legs, each leg must be scaled appropriately. In considering the size of an optical system, it is also important to account for the turbulence strength. The most direct way of scaling atmospheric turbulence is through the coherence length, r_0. In particular, by keeping the ratio of the source diameter to r_0 constant (i.e. $\frac{D}{r_0} = constant$), the system's behavior is preserved when scaling from one size to another. For example, an optical system with a source diameter of $25cm$ operates in turbulence with an r_0 of $10cm$. A simulation system with an aperture of $2.5cm$ is used to analyze the scenario. In order to obtain an accurate representation, r_0 for the turbulence must be $(10cm/25cm) \times 2.5cm = 1cm$. These scaling concepts must be taken into account when converting from a real scenario to the small-scale lab simulation.

2.8 Sampling

When simulating using discrete calculations care must be taken in choosing the correct sample spacing and wavefront extent for initial and final wavefronts. One challenge is that a given wavefront can have dissimilar spatial frequency behavior in amplitude and phase, but only one sample period is used to adequately represent both amplitude and phase. The amplitude must be sampled at a minimum of 2 times the highest spatial frequency to satisfy Nyquist criterion. At the same time, the phase must be sampled with a high enough frequency such that the change from one phase

sample to the next is not greater than π radians. Phase representation is modulo 2π when using the Fresnel Integral. For this reason, phase changes that jump from one sample to the next by more than π can be misconstrued as, for example, an increase in phase from the first sample to the next, when in reality, a decrease in phase occurred. Setting the physical extent of the grid that describes the field will also have an effect on the accuracy of the simulation. The grid size at the output plane after a propagation must be large enough to represent all relevant light incident on the plane. It must also be large enough to avoid frequency wrap around affects caused by the Fourier transform algorithm used to propagate the light. Specifically, if λ is the wavelength of light and dx is the sample period used to represent the field, the diffraction angle of light exiting one sample point is $\frac{\lambda}{dx}$. If the propagation distance is z, the light from one sample point covers a length at the output plane of $\frac{\lambda z}{dx}$. The above relationships can be used to formulate a rule for choosing a sample period. Specifically, if prior knowledge exists about the size of the grid that one would like to observe at the receiver plane, a necessary sample spacing to prevent aliasing would be an area with length of both the source and receiver combined. So the sample spacing would be:

$$d_{xy} = \frac{\lambda z}{D_{source} + D_{receiver}} \tag{2.29}$$

The grid size at the output plane should in general be $2\frac{\lambda z}{dx}$ to allow enough space to view the propagated light while not experiencing wrap-around effects from the Fourier transform used in the Fresnel integral. Further, the diameter of the source can be related to the previous relationship to determine the necessary grid size:

$$size_{grid} = D_{source} + \frac{\lambda z}{d_{xy}} \tag{2.30}$$

where D_{source} is the diameter of the source and d_{xy} is the sample spacing chosen for the propagation. Equation 2.30 is a rule of thumb that may not guarantee absence of wrap-around if propagating a large distance with a small source diameter. In

all simulations discussed later these sampling requirements were used to set grid parameters.

2.9   System Evaluation

While evaluating system performance in producing atmospheric perturbations, it is necessary to measure the Fried parameter, the isoplanatic angle and the Rytov variance defined by equations 2.20, 2.21, and 2.22 respectively; however we can only directly measure intensity and relative phase across the wavefront.

2.9.1   Measuring r_0.

Solving equation 2.14 for r_0 produces

$$r_0 = \left[\frac{6.88 R^{5/3}}{D_n(R)} \right]^{3/5} \tag{2.31}$$

It should be clear that if we can recreate the structure function in the inertial subrange we can estimate r_0. In order to make this measurement the wavescope wavefront sensor is used to capture a series of phase fronts. A structure function is found for each of these phase fronts and then the structure functions are averaged.

2.9.2   Measuring σ_1^2.

A known benchmark concerning intensity is used called the lognormal distribution. This intensity distribution is given by

$$p(I) = \frac{1}{2\sqrt{2\pi}I\sigma_\chi} \exp\left[-\frac{\left(\ln\frac{I}{A^2} - 2\langle\chi\rangle\right)^2}{8\sigma_\chi^2} \right] \quad , \quad I > 0 \; , \tag{2.32}$$

where I is the intensity, A is the unperturbed field's amplitude, and σ_χ and $\langle\chi\rangle$ are parameters of the distribution.

The lognormal distribution stems from one classical theory of optical wave propagation called the Rytov approximation. It builds on small fluctuations in refractive index as multipliers to the unperturbed wave [1]. The lognormal distribution is accurate only in a "weak fluctuation" regime. For the atmospheric model to exist in the weak fluctuation regime, its Rytov variance (equation 2.22) must be: $\sigma_1^2 < 1$ [1].

Therefore, in measuring the output intensity of the optical system under test, a log-normal intensity distribution is expected for a single pixel over many phase screens.

In the *weak fluctuation* regime the lognormal distribution can be rewritten in term of the scintillation index, σ_I:

$$p(I) = \frac{1}{\sqrt{2\pi} I \sigma_I} \exp\left[-\frac{\left(\ln \frac{I}{\langle I \rangle} + \frac{1}{2}\sigma_I^2\right)^2}{2\sigma_I^2} \right] \quad , \quad I > 0 \ , \tag{2.33}$$

Since the scintillation index can be analytically determined from the Rytov variance, σ_1^2, intensity pdf data can be collected to determine the Rytov variance of the scenario under test [2].

III. Methodology

3.1 Introduction

Using the theory from chapter 2 as a starting point it is possible to build a hardware atmospheric simulator. The simulator to be demonstrated will consist of two SLM phase screen generators, a CCD camera, a wavefront sensor, and all necessary optics.

3.2 SLM

3.2.1 SLM Description. The SLM used in this research is a 512 by 512 pixel phase-only reflective SLM built by Boulder Nonlinear Systems. Each pixel has a pitch of 15 μm, and the total array size is 7.68 mm; the SLM has a fill factor of 83%. This fill factor being less than unity gives a maximum diffraction efficiency of 61.5% [3], where diffraction efficiency is defined as the amount of light in the zero order diffraction lobe.

3.2.2 SLM Calibration. Before a SLM can be used it must be properly calibrated to determine the phase delay associated with each voltage value applied to each pixel. In order to calibrate the phase response of the SLM a Twyman-Green interferometer (see Figure 3.1) was setup in the lab. Here, a monochromatic collimated light source (laser beam expanded so it is larger than the diagonal of the SLM) passes through a non-polarizing beamsplitter plate such that the beam is divided into two beams, with nearly equal intensity. One of these beams illuminates the XY Phase Series SLM, while the other illuminates a Reference Mirror. Each of the reflected beams is then recombined at the Image Plane of a Lens. A camera is placed at the image plane in order to capture the fringes for easier processing. If the Reference Mirror and the SLM are carefully aligned such that they are nearly coplanar and the optical path length difference is less than the coherence length of the laser, interference fringes will be visible at the Image Plane. By carefully adjusting the amount of tilt on the reference mirror the number of fringes visible in the image plane can be adjusted.
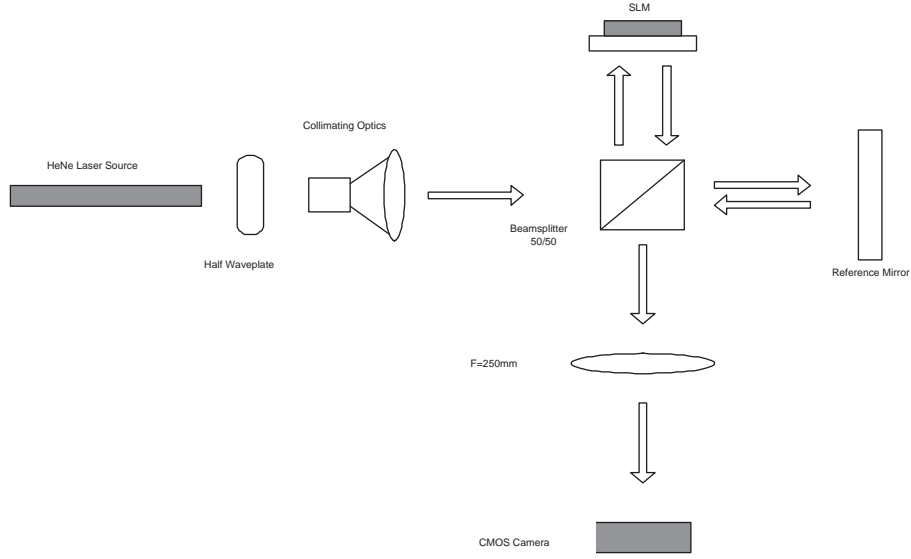
Figure 3.1:   Twyman Green Interferometer used for SLM Calibration.

When the XY Phase Series SLM is driven with different phase patterns, dynamic interference fringes can be viewed [3]. Analyzing the interference fringes will then provide insight into the phase modulation provided by the XY Phase Series SLM. In order to accurately measure phase shift it is necessary to use high quality optics; the beam splitter plate used is flat to $\lambda/20$ and the reference mirror is flat to $\lambda/10$.

The SLM is calibrated by applying flat gray values to the SLM and recording an intensity value for a small portion of the image plane. As these gray values are changed, which adds a phase delay to one leg of the interferometer, the fringes, as seen in Figure 3.2, will move across the camera creating an intensity modulation in the image plane. If we assume for a moment that the laser coherence length is infinite, which in the frame of our experiment is a reasonable assumption, then the interference pattern can be viewed as an infinite series of sinusoidal fringes [7]. This allows us to relate the intensity pattern measured at the camera to a phase delay in waves given by:

$$delay = \frac{\cos^{-1}\sqrt{I}}{\pi} \qquad (3.1)$$
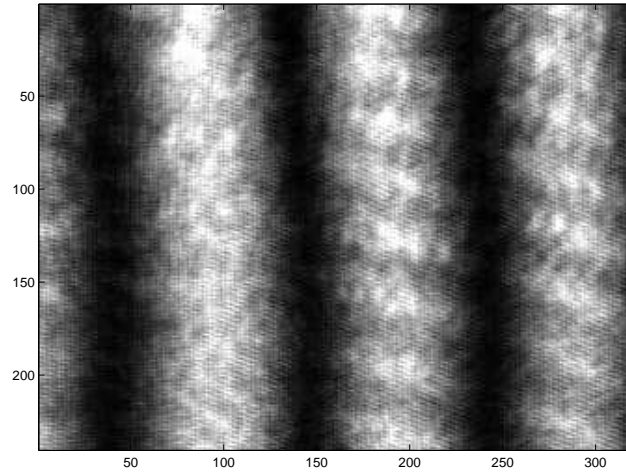
Figure 3.2:   Sample Interferogram from Twyman Green Interferometer.
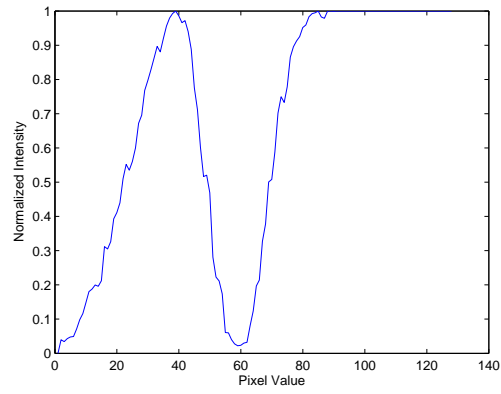

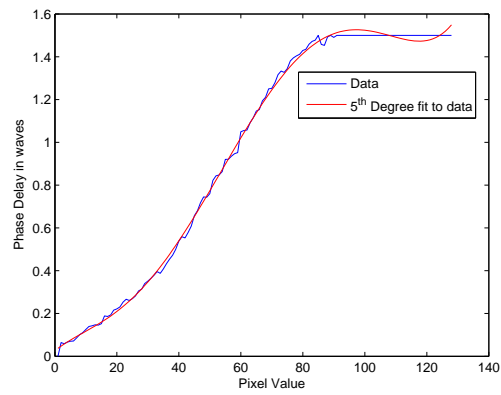Figure 3.3:   Intensity Variation vs Gray Values for SLM 1.

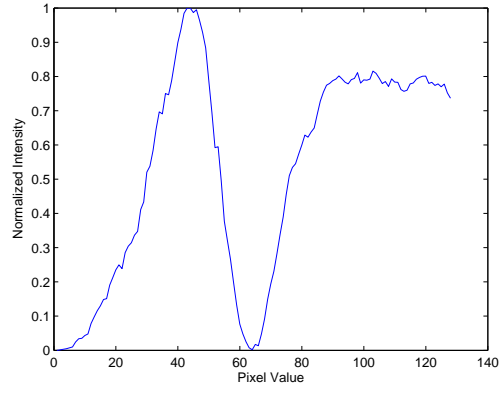Figure 3.4:   Phase Delay vs Gray Values for SLM 1.

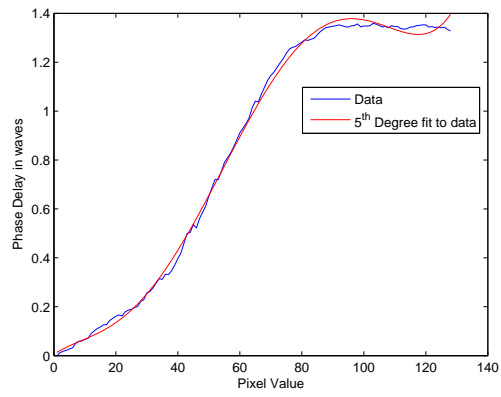Figure 3.5:   Intensity Variation vs Gray Values for SLM 2.

Figure 3.6:   Phase Delay vs Gray Values for SLM 2.

30

When viewing the interference pattern from the interferometer set up seen in Figure 3.1, the expected fringes will be seen along with a set of secondary fringes. These secondary fringes result from multiple reflections in the beamsplitter plate and will have no effect on the calibration process.

The results of the SLM calibrations can be seen in Figures **??** - 3.6.

3.2.3   Other SLM Concerns.   As previously mentioned the SLM has a fill factor of only 83% which means only a portion on the light incident on the SLM can be controlled in a predictable fashion. The amount of light that is uncontrolled (as a result of being incident between pixels) will be smaller than 17% since the field lines are not going to have a sharp cutoff at the electrode edges; however if the controlled light is tilted off axis it may be possible to eliminate any interference effects caused by the uncontrolled light, which will remain in the zero order diffraction spot. To accomplish this 134 waves of tilt (95 waves in x and 95 waves in y) were added to each turbulence screen; 134 waves at $632.9nm$ gives a steering angle of $14.1\mu rad$. Since the screens represent the phase delay modulo 2π the tilt screens act as a diffraction grating sending light into multiple high order tilted spots. The size of the grating is small so the diffraction angle is large enough to allow the high order spots to be ignored since they are diffracted out of the field of view.

In some cases it is not possible to eliminate these effects due to the distance from the SLM being too small to separate the steered and unsteered light. The effects were found to be minimal since the amount of uncontrolled light is small. Another concern is the SLM housing causes light to be scattered from the edges and in some cases it is necessary to mask the edges to avoid this scatter. These to effects can be clearly seen in Figure 3.7; the reflection with edges masked can be seen in Figure 3.8.

A final concern with the SLMs is whether they can represent the appropriate spatial frequency content of the turbulence scenarios. The Nyquist theorem says that at least two samples are required per period of the highest spatial frequency
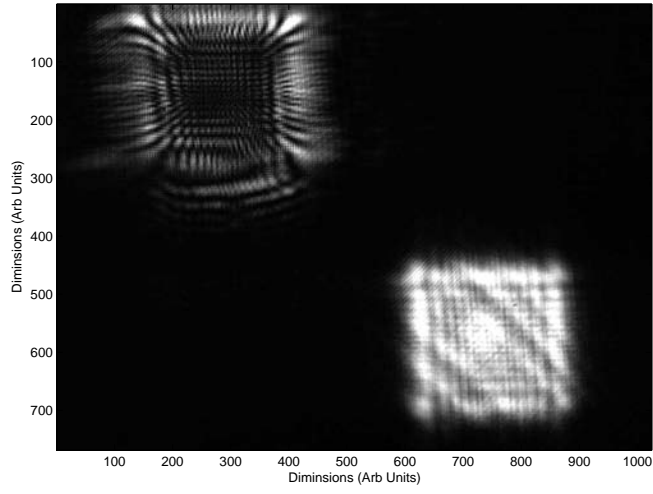
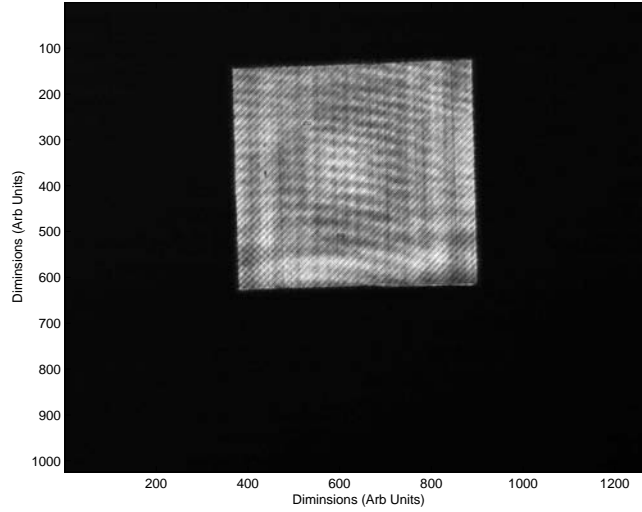Figure 3.7:   Reflection from first SLM with 95 waves of tilt in x and y.

Figure 3.8:   Reflection from SLM with the edges masked to eliminate scattering from the SLM housing. Note that the zero order spot is out of the field of view.
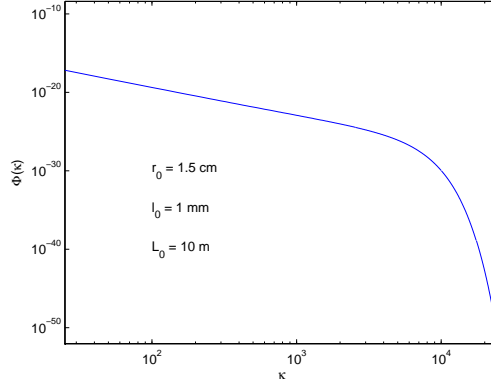
Figure 3.9:   PSD for atmosphere with $r_0 = 1.5cm$.

component to accurately reproduce a signal. Since the SLM pixel pitch is $15\mu m$, the maximum spatial frequency that can be represented is $3.33 \times 10^4 m^{-1}$ in both x and y. The 95 waves of tilt added in each direction uses a portion of this spatial frequency, however $2.10 \times 10^4 m^{-1}$ is still available to represent our turbulence cases. As can be seen in Figure 3.9 the amount of power contained in spatial frequencies higher than this is insignificant for moderate turbulence; very turbulent atmosphere may require higher spatial frequencies. The effects are further minimized since the simulated atmosphere is broken into multiple screens, since it requires less spatial frequency to represent a weaker turbulence case and each screen is effectively a weaker case than the total.

3.3   System Set up and Operation

3.3.1   Optic Bench Setup.   The lab experiment (seen in Figure 3.10) consists of a collimated He-Ne laser source reflected from two SLMs and into a sensor. A half wave plate (or linear polarizer) is placed before the first SLM and also between the two SLMs. The half wave plates are used to rotate the linear polarization from the He-Ne into the proper frame for the SLM. The spacing of the two SLMs is crucial to our system model. Each propagation leg is scaled using Fresnel numbers to match the corresponding leg in the atmospheric scenario. A lens is used to image the desired output plane onto the camera for intensity measurements. The location of the output
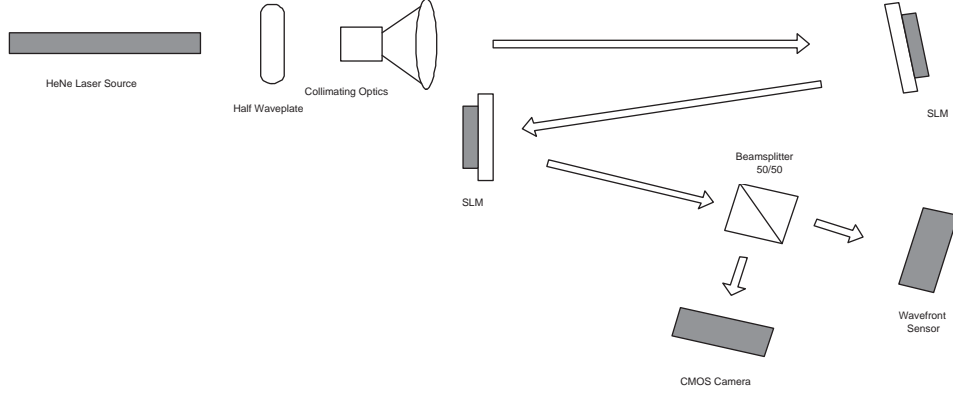
Figure 3.10:   Experimental Setup for a two phase screen turbulence generator.

plane in phase measurements in not important so the lens was removed and the wavefront sensor placed in the beam path at an arbitrary location.

The wavefront sensor is a Wavescope 2.0 from Adaptive Optics Associates, Inc. The wavefront sensor has an input aperture populated with lenslets which effectively produce an array of Hartmann sensors. The idea of a Hartmann sensor is that each lenslet focuses a portion of the wavefront onto a quad detector. If the wave is tilted the light is focused off center in the quad detector and the distance off center is used to calculate the local tilt. The local tilt in each subaperture are then recombined by mathematical algorithms to represent a continuous wavefront.

The array of lenslets allows the entire wavefront to be sampled simultaneously, and accurately reconstructed provided it was sampled at the proper rate. Three lenslet arrays are available for the wavescope; the lenslet pitch for each array is: 480 μm, 300 μm, and 133 μm. The 300 μm pitch array was chosen for this experiment. Each scenario should only yield a few waves of tilt across the receiving aperture so the 300 μm array will more than satisfy the phase sampling criteria.

The target board is a CMOS ultra camera built by Computer Modules, Inc. The camera has a 1280 by 1024 array with a pixel pitch of 7.5 μm. The camera is also supplied with a simple software package for interface to a PC. The software allows

the user to select camera integration time and the area of interest on the array. The software also performs frame averaging.

 3.3.2   Operation.   In order to simulate atmospheric turbulence, phase screens must be applied to the SLMs. These screens are created in Matlab using the Fourier series method and saved as bitmaps. The Blink software provided with the SLMs is used to load the phase screens. Laser light is then passed through the system and captured at the sensor. The phase screen is then changed and the process repeated. For each scenario 1000 frames of intensity data and 200 frames of phase data were captured and processed.

3.4   Computer Simulation

 Computer simulation was performed using Wavetrain (see Figure 3.11), a wave optics code produced by MZA Associates Corporation in Albuquerque, New Mexico. Using Wavetrain it was possible to model the atmospheric scenarios of interest. Wavetrain allows for parameters to be varied in order to perform parameter studies; in this research, system parameters (aperture size, wavelength, and detector specifications) and propagation path length were fixed and turbulence parameters were allowed to vary. Wavetrain allows atmospheric turbulence to be specified in several formats, the most flexible of which allows for specification of number of phase screens, as well as the location and strength of each screen. This was the format chosen for this effort.

 An additional simulation was performed in Matlab to isolate the effects of diffraction through a square aperture. The code uses Fresnel propagation algorithms to propagate a incident plane wave beyond a single square aperture. The simulation was repeated to show the compounding effects of two sequential square apertures spaced two meters apart. Results are discussed in Chapter 4.
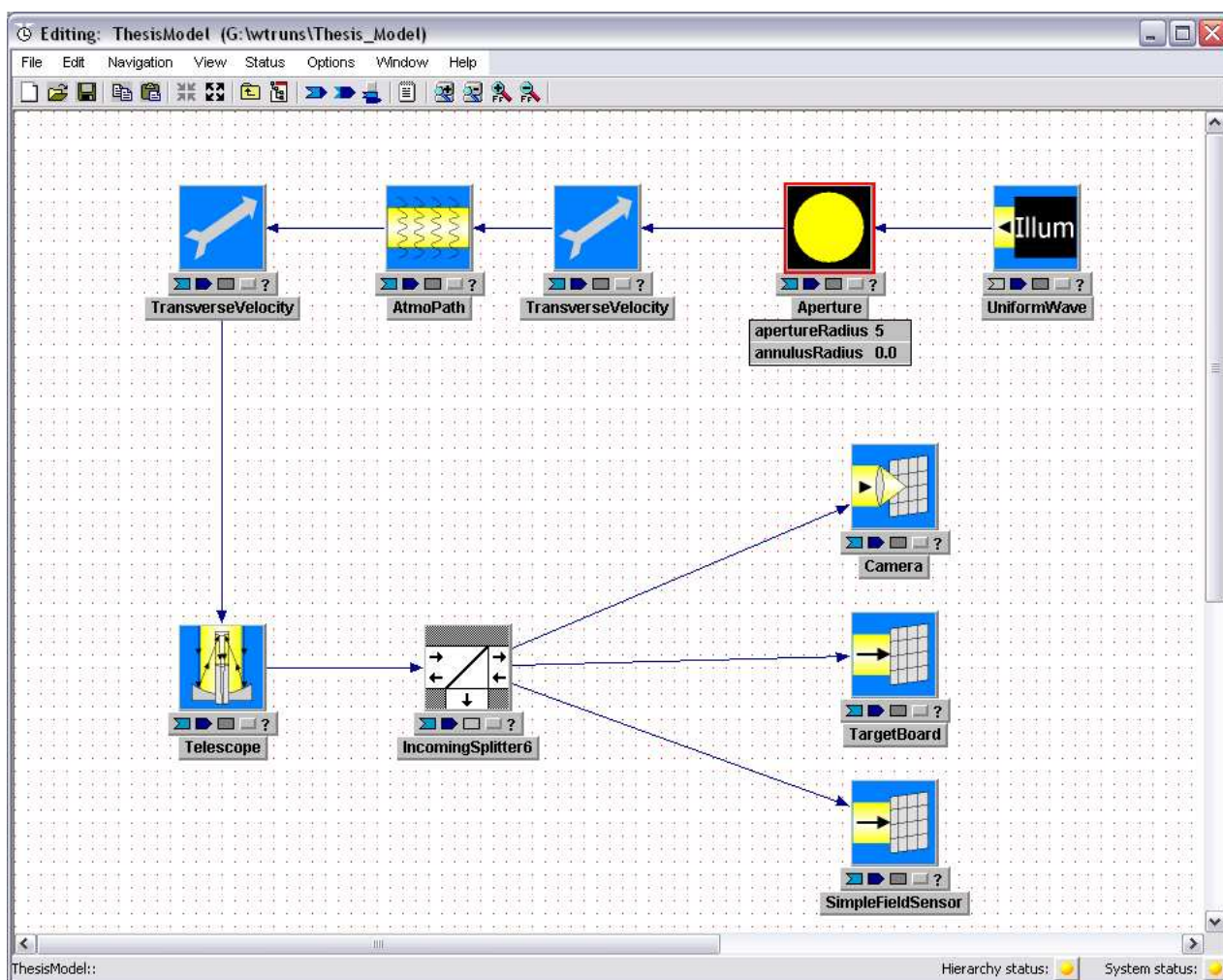
Figure 3.11:   Wavetrain Simulation model layout.

3.5 Summary

The phase response of the SLMs for this experiment was calibrated and a two phase screen atmospheric simulator was constructed. Phase screens were then loaded onto the SLMs and output parameters were collected. These output parameters were intensity and phase profiles as a function of space and time. The data was then used to create intensity PDFs and phase structure functions to validate performance of the system. The atmospheric scenarios were also modeled in Wavetrain. The two data sets were then compared to each other as well as to theory.

IV. Analysis and Experimental Results

4.1   Introduction

The system described in Chapter 3 was used to apply atmospheric abberations onto a collimated laser beam. The quality of this simulation is limited by the SLM hardware and our ability to create representative phase screens. In order to validate the system it is necessary to first look at the statistics of the screens used; this will determine the validity of our system input. The screens are created differently in the experiment and the simulation, but this will be discussed more later. Further system validation will be accomplished by collecting the statistics of light that is passed through the screens; phase and intensity statistics will be collected and analyzed. After looking at the collected data in both simulation and experiment the dominant error source is identified and discussed.

In section 4.2 the scenarios of interest will be described in detail; section 4.3 lays out the analytical solution. The analysis is founded in the theory from chapter 2. Section 4.4 details a wavetrain implementation of the analytical model; while section 4.5 described the experiment and results.

4.2   Scenarios

In this research all scenarios considered will be a receiver located on the ground and looked at star at zenith (plane wave). The only things we will vary are the turbulence strength parameters. Five scenarios will be examined and can be found in Table 4.1.

Table 4.1:   Test scenario parameters

Scenario	D/r_0 Ratio	Real r_0	Lab r_0
1	7.582	6.595cm	0.1013cm
2	3.303	15.14cm	0.2326cm
3	5.047	9.906cm	0.1522cm
4	19.372	2.581cm	0.0396cm
5	32.072	1.559cm	0.0239cm

Table 4.2: Detailed scenario descriptions

Scenario	Screen 1 Location	Screen 1 r_0	Screen 2 Location	Screen 2 r_0	σ_1^2
1	250m	6.892cm	10km	32.314cm	0.179
2	250m	16.868cm	10km	44.673cm	0.08
3	250m	10.337cm	10km	49.568cm	0.088
4	100m	2.634cm	9.85km	20.042cm	0.401
5	100m	1.566cm	9.85km	29.398cm	0.502

4.3 Analysis

This section contains the analytic model used in this research. It shows, based on theory, that it is possible to accurately model atmospheric scenarios using two phase screens.

4.3.1 Continuous Model. The Hufnagel-Valley atmospheric model (ref Eq 2.19) is used to describe the $C_n^2(h)$ profile for this research; the parameters A and v will be varied to satisfy our scenario values. Other model parameters of interest are: $\lambda = 633nm$ and $L = 30km$ where λ is wavelength and L is total propagation length.

For the continuous atmospheric model equations 2.20, 2.21 and 2.22 can be used to find the values of the atmospheric parameters of interest. Since the continuous model most closely represents reality it will be used as the truth model.

4.3.2 Two Screen Model. For the two screen model additional parameters must be defined: h_1 is the height of the first phase screen, h_2 is the height of the second phase screen, and Δh is the height of the boundary between turbulence layers represented by each screen. The only parameter the will be allowed to vary is Δh, which will effectively change the strength of each screen. Each screen can be represented by an average $C_{n,i}^2$ value for that screen defined by:

$$C_{n,1}^2 = \frac{\int_0^{\Delta h} C_n^2(h)dh}{\Delta h} \tag{4.1}$$

$$C_{n,2}^2 = \frac{\int_{\Delta h}^{L} C_n^2(h)dh}{L - \Delta h} \tag{4.2}$$

This notation gives a discrete representation of the continuous $C_n^2(h)$ profile. Since C_n^2 has been modeled as a discrete sum of two values, equations 2.20, 2.21 and 2.22 can be written as:

$$r_0 = 1.67 \left[k^2 \sum_{i=1}^{2} C_{n,i}^2 \Delta h_i \right]^{-3/5} \tag{4.3}$$

$$\theta_0 = \left[2.91 k^2 \sum_{i=1}^{2} h_i^{5/3} C_{n,i}^2 \Delta h_i \right]^{-3/5} \tag{4.4}$$

$$\sigma_1 = 2.25 k^{7/6} \sum_{i=1}^{2} C_{n,i}^2 h_i^{5/6} \Delta h_i \tag{4.5}$$

where h_i and Δh_i are the height and thickness of each turbulence layer and can be found by:

$$
\begin{aligned}
h_1 &= 1km \\
h_2 &= 10km \\
\Delta h_1 &= \Delta h \\
\Delta h_2 &= L - \Delta h
\end{aligned}
$$

$$\tag{4.6}$$

It is also necessary to calculate a r_0 value for each screen; these values are found by:

$$r_{0,1} = 1.67 \left[k^2 \int_0^{\Delta h} C_n^2(z) dz \right]^{-3/5} \tag{4.7}$$

and

$$r_{0,2} = 1.67 \left[k^2 \int_{\Delta h}^{L} C_n^2(z) dz \right]^{-3/5} \tag{4.8}$$

These values, $r_{0,1}$ and $r_{0,2}$, are necessary because they will be used as input values to the turbulence screen generation algorithm.

4.4 Computer Simulation

Simulations were performed to mimic the atmospheric scenarios that would be created in the lab. The output of these simulations was processed to yield a intensity PDF and a phase structure function for each scenario. Simulation yielded acceptable results, in that it followed the expected form of the output (lognormal for PDF and 5/3 power law for structure functions). However, it did have some deviations from theory that need to be examined.

For a complete simulation description see section 3.4. In the simulation the phase screen locations and strengths were assigned according to Table 4.2.

4.4.1 PDF Evaluation.

Intensity PDFs were created in order to verify that Rytov variance could be properly modeled using only two phase screens in a propagation path. Since the data was being used as a measurement of Rytov variance, σ_1^2, the percent error was defined in terms of theoretical Rytov variance, $\sigma_{1\,theory}^2$, and the measured Rytov variance, $\sigma_{1\,measured}^2$

$$PercentError = \frac{|\sigma_{1\,theory}^2 - \sigma_{1\,measured}^2|}{\sigma_{1\,theory}^2} \qquad (4.9)$$

The PDFs were created by cycling through 5000 sequential screens, which were created by Wavetrain using the Fourier series technique; a single pixel value is stored from the intensity pattern resulting from each screen. By capturing the intensity from the center pixel as a number of screens sequence it is possible to create a temporal PDF of intensity.

Figures 4.1 - 4.5 show the results of the simulations. In the figures three curves are plotted: a theoretical curve, a data curve, and a best fit curve. The theoretical curve is a plot of the lognormal distribution that is predicted for the PDF in the weak turbulence regime; the data curve is a histogram of intensity data from the simulation. The best fit curve is created by finding the mean and variance of the data and plotting a lognormal distribution using those values as inputs. Errors for each
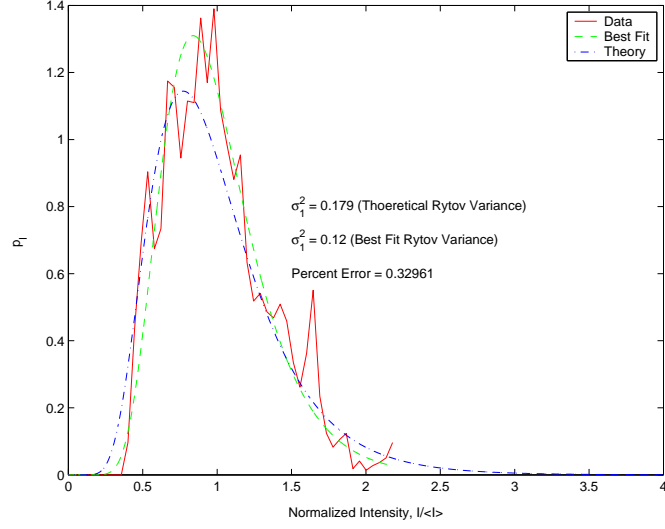
Figure 4.1:   Scenario 1 Simulation PDF results.

scenario are 32.5%, 27.5%, 34.1%, 25.0%, and 44.0% respectively, while these seem large it does not take a large error in mean or variance of the output data to yield these results. It is also important to note that the analytical Rytov variance is higher than the measured for every case. This means that the simulation turbulence is, in a sense, weaker than expected. When Wavetrain creates phase screens the spatial frequency is linearly sampled; this will under-represent the tilt variance, therefore under representing total turbulence strength. This under representation is seen as a lower Rytov variance.
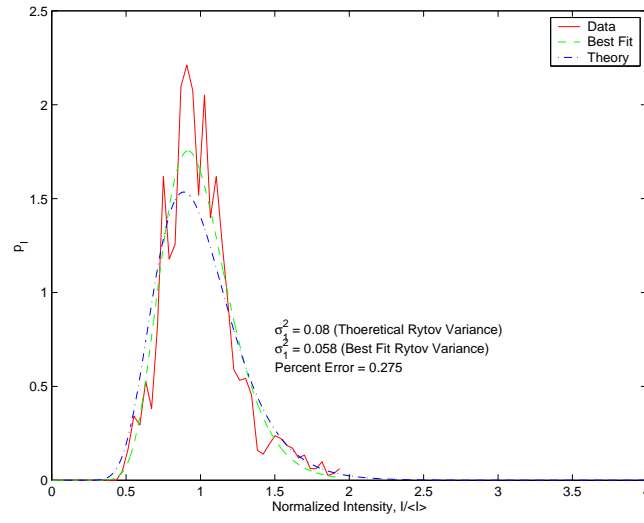
Figure 4.2:   Scenario 2 Simulation PDF results.
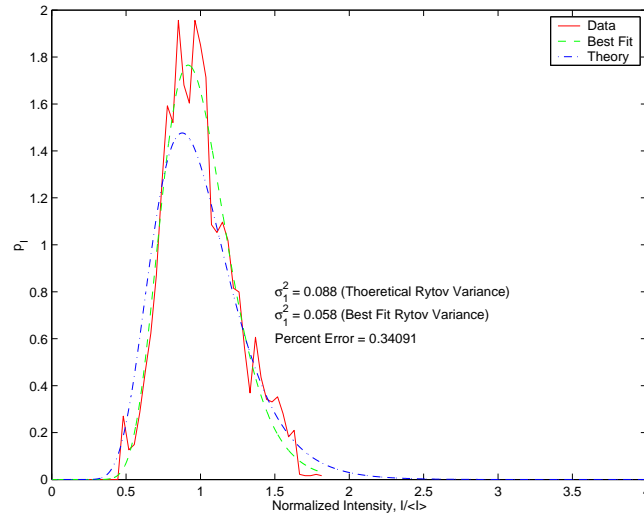
Figure 4.3:   Scenario 3 Simulation PDF results.
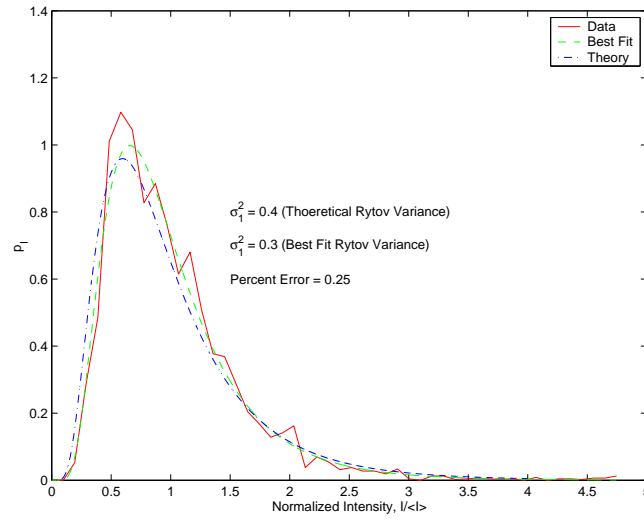
Figure 4.4:   Scenario 4 Simulation PDF results.
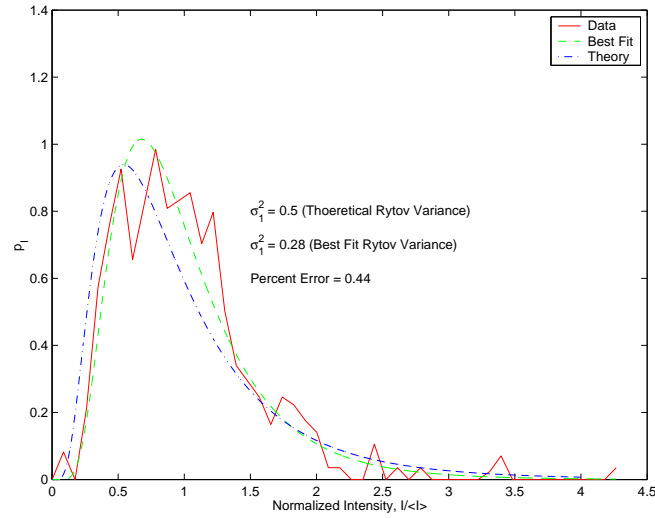
Figure 4.5:   Scenario 5 Simulation PDF results.

4.4.2 Structure Function Evaluation.   Phase structure functions were cre-
ated to measure r_0 for each scenario. To create the structure functions 200 screens
were cycled and the wavefront was captured using Wavetrain's simple field sensor.
Structure functions are calculated for each output wave and then averaged. In each
structure function a drop off can be seen at large separations; this is a by product
of the linear frequency sampling mentioned earlier. If screens are generated using
logarithmical spaced spatial frequency samples this drop off would be much less pro-
nounced.

Since the structure functions are used to measure r_0 we define our error as

$$PercentError = \frac{|r_{0theory} - r_{0measured}|}{r_{0theory}} \qquad (4.10)$$

Plots of the measured structure functions can be found Figures 4.6 - 4.10. Like the
PDF curves above the structure function plots also show data, theory, and a best
fit. The data curve is a plot of the calculated structure function resulting for the
simulation data; the theory curve is plotted using the predicted r_0 and equation 2.14;
the best fit curve for the structure function was created by cycling through different
values of r_0 and selecting the one that most closely matched the data. It should be
noted that more emphasis was put on fitting for small separations; the reason for this
follows from the dip at large separations which results from undersampling the low
spatial frequency content of the phase screen PSD.

Errors for each case are 0% (within the measurement precision), 33.9%, 19.2%,
35.6%, and 15.5% respectively; recall from equation 4.10 that margin of error is based
on the difference between theory and best fit. One trend of note is that for weaker
turbulence (cases 2 and 3) r_0 is smaller than expected (stronger turbulence) while for
very strong turbulence (cases 4 and 5) r_0 is larger than expected.
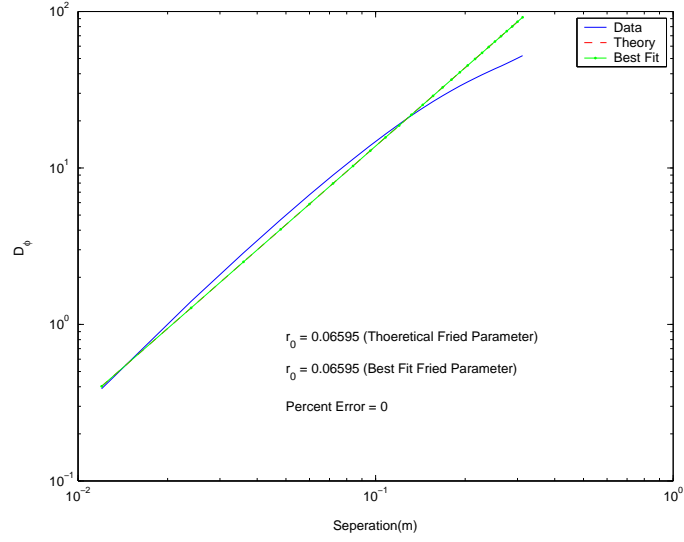
Figure 4.6:   Scenario 1 Simulation Phase Structure Function.
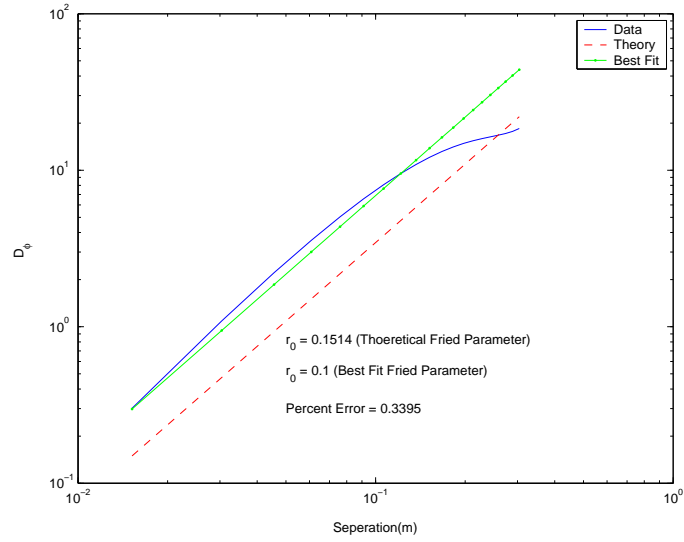

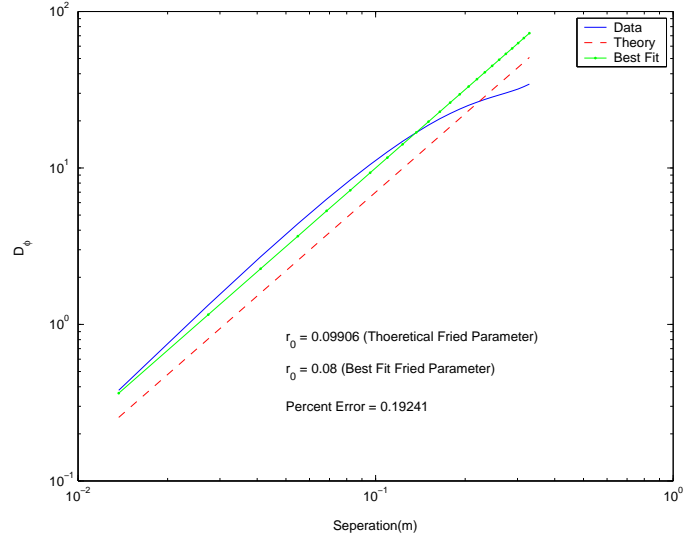Figure 4.7:   Scenario 2 Simulation Phase Structure Function.

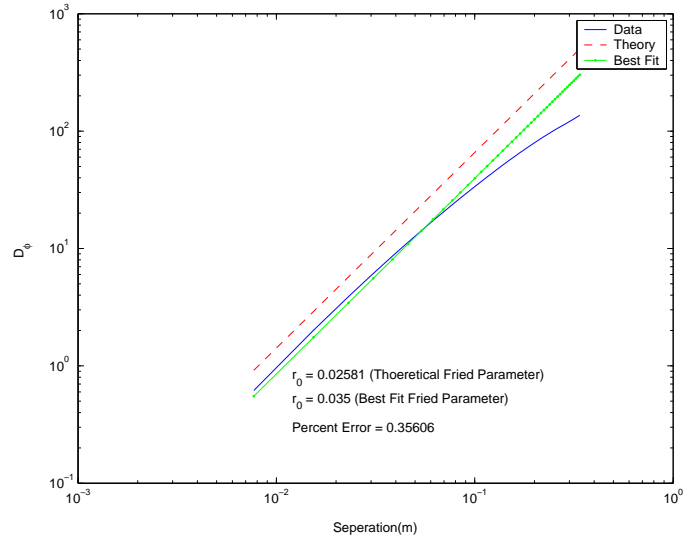Figure 4.8:   Scenario 3 Simulation Phase Structure Function.

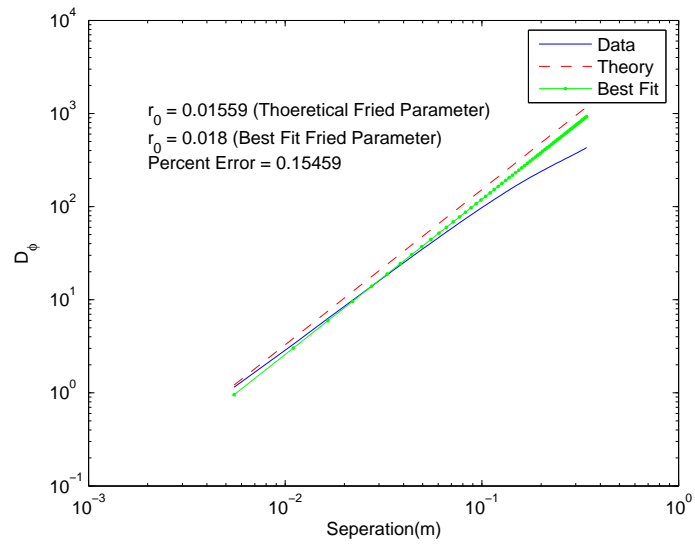Figure 4.9:   Scenario 4 Simulation Phase Structure Function.

Figure 4.10:   Scenario 5 Simulation Phase Structure Function.

Table 4.3: Detailed scenario descriptions

Scenario	Screen 1 Location	Screen 1 r_0	Screen 2 Location	Screen 2 r_0	σ_1^2
1	5.9cm	0.1059cm	2.359m	0.4963cm	0.179
2	5.9cm	0.2591cm	2.359m	0.6862cm	0.08
3	5.9cm	0.1588cm	2.359m	0.7614cm	0.088
4	2.36cm	0.0405cm	2.3236m	0.3078cm	0.401
5	2.36cm	0.0241cm	2.3236m	0.4516cm	0.502
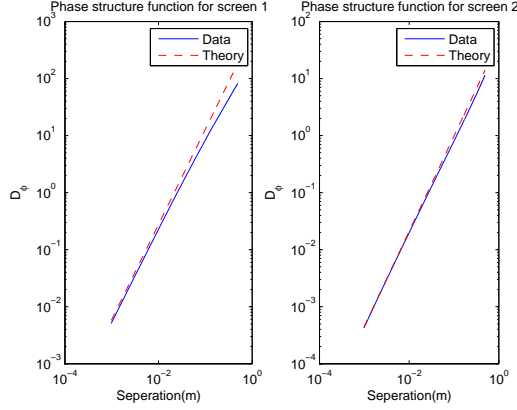
Figure 4.11: Scenario 1 Screen Structure Function results.

4.5 Experimental Results

In this section the results from the laboratory experiments are discussed. The same scenarios are used from the simulation, but they were scaled for smaller aperture size and propagation lengths. The scaling was done by matching the lab Fresnel number to the atmospheric Fresnel number. The resulting scenario parameters can be found in Table 4.3. In the table all locations are measured from the camera.

4.5.1 Screen Validation. Phase screens were created in Matlab using the Fourier Series method. To verify that screens are being created properly structure functions were calculated. The structure functions of the screens are found in Figures 4.11 - 4.15. It is clear from the plots that the screens accurately represent the desired statistics. It should also be pointed out that the PSD used to create the screens was sampled using a logarithmical method, therefore the dip at the large separations is almost entirely eliminated.
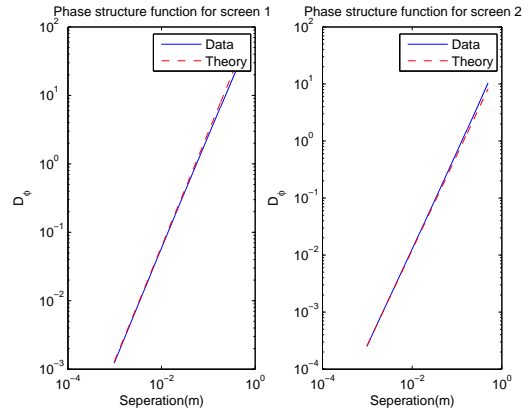
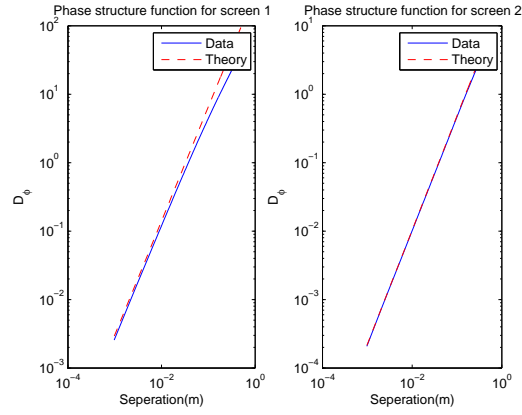Figure 4.12:   Scenario 2 Screen Structure Function results.

Figure 4.13:   Scenario 3 Screen Structure Function results.
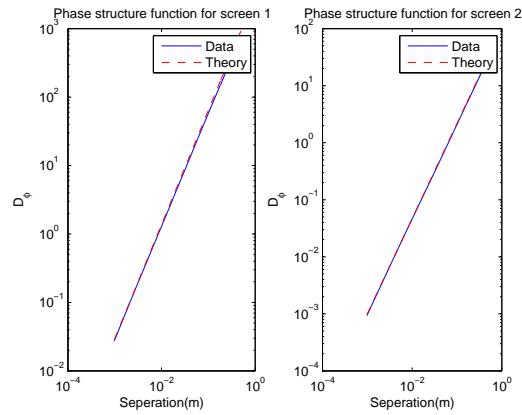

Figure 4.14:   Scenario 4 Screen Structure Function results.
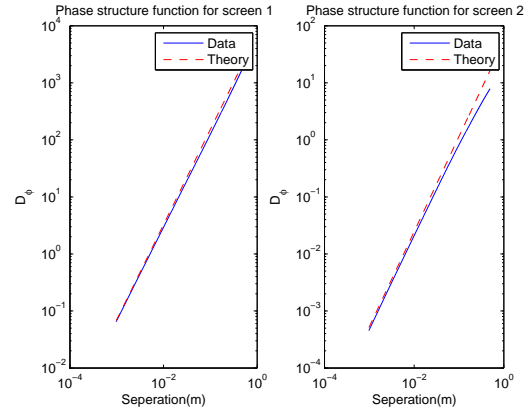
Figure 4.15:   Scenario 5 Screen Structure Function results.

4.5.2 PDF Evaluation.   The temporal PDF on intensity was measured in the lab by sequencing 1000 screens and collecting intensity data at a single pixel, in the same manner as the simulation discussed above. In order to assure accurate results care must be taken when setting up the camera. The integration time must be adjusted short enough to avoid ever saturating any pixels, but long enough to take advantage of all the possible output values of the 8 bit camera. If the camera does saturate you will get many data points equal to the saturated value therefore the data is no longer valid.

Figures 4.16 - 4.20 show the PDF results collected in the experiment. These figures contain the same three curves as the simulation PDF data.

Recalling equation 4.9 errors for each case are 2.2%, 75.0%, 36.4%, 30.0%, and 44.0%. A trend that should be pointed out is that the system tends to create Rytov variance higher than expected for very weak turbulence, a Rytov very close to expected for moderate turbulence, and a Rytov variance lower than expected for stronger turbulence cases. The suspected sources of error for this measurement are: (1) data being measured in the wrong output plane, (2) camera limitations, (3) and diffraction from the square aperture. Camera limitations, such as low intensity resolution and noise, will not be discussed here. Diffraction has a limited effect on the PDF since the diffraction pattern from the aperture is stationary; diffraction has much more impact on the structure function and will be discussed in a later section. Data measurement in a plane other than the plane of interest is a predominant source of error in these measurements. Recalling equation 4.5 it can be seen that the Rytov variance is the $h^{\frac{5}{6}}$ moment of C_n^2. As a result the value measured is sensitive to the plane where it is measured.
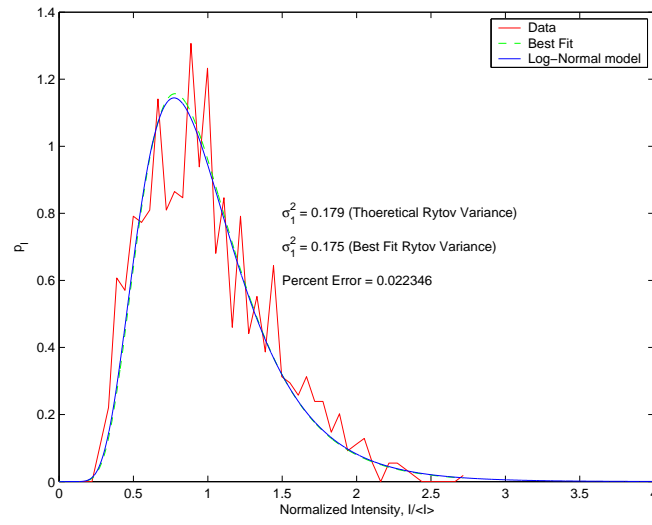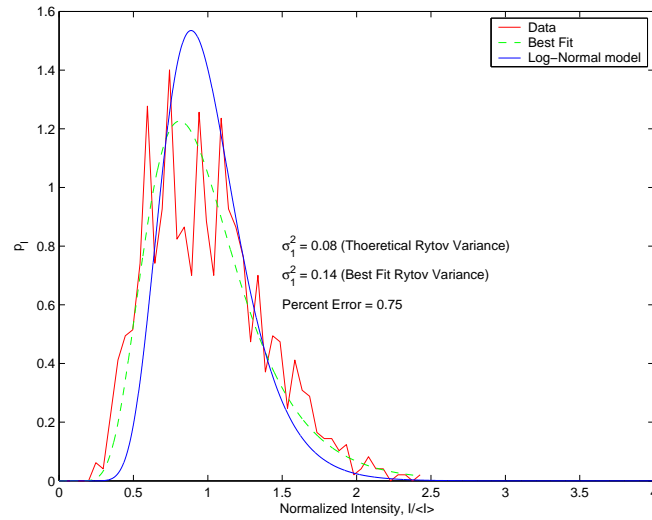
Figure 4.16:   Scenario 1 PDF results.

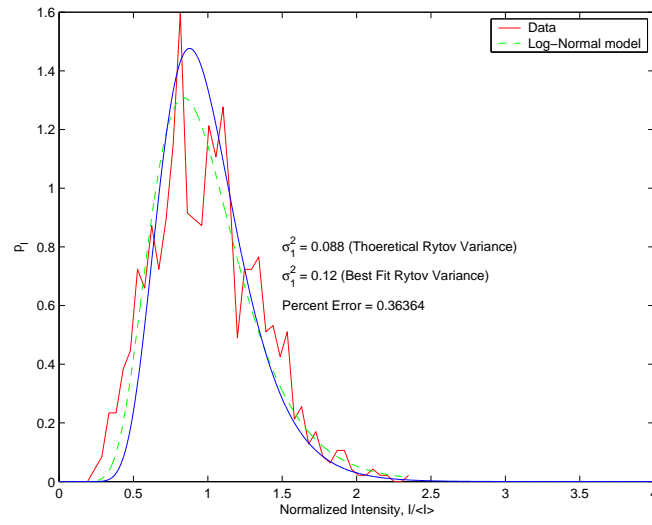Figure 4.17:   Scenario 2 PDF results.

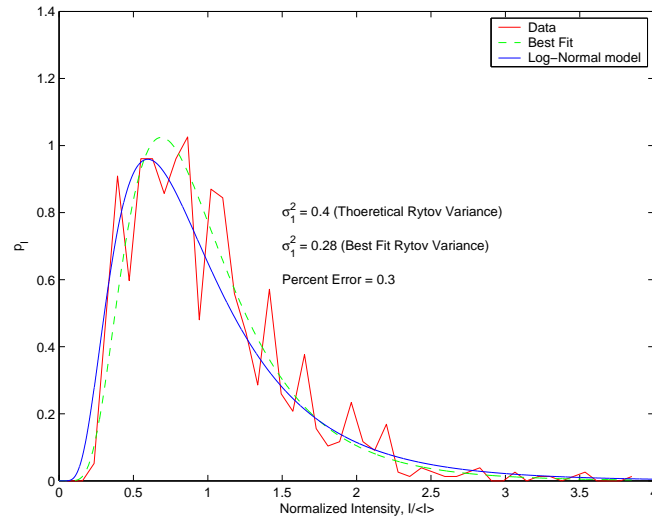Figure 4.18:   Scenario 3 PDF results.

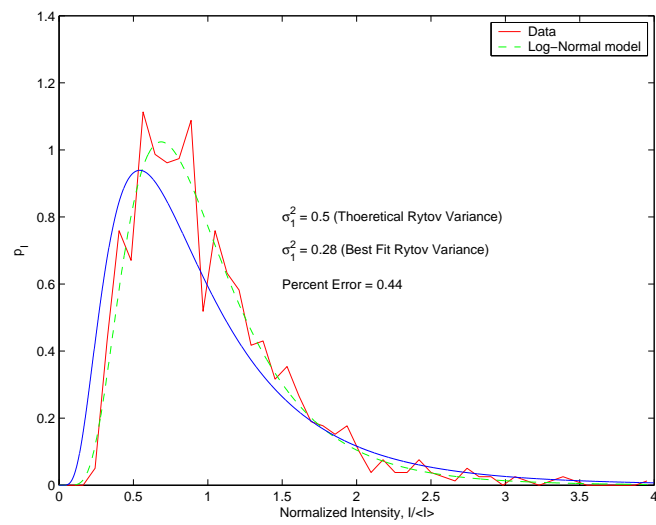Figure 4.19:   Scenario 4 PDF results.

Figure 4.20:   Scenario 5 PDF results.
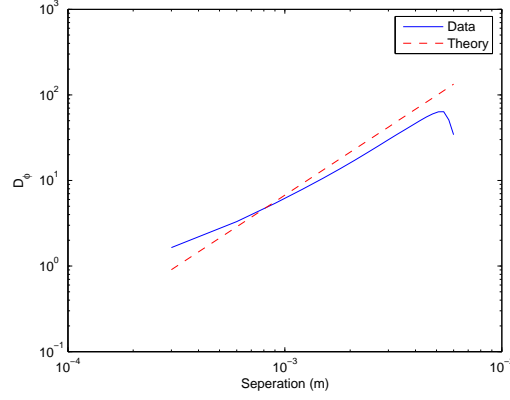
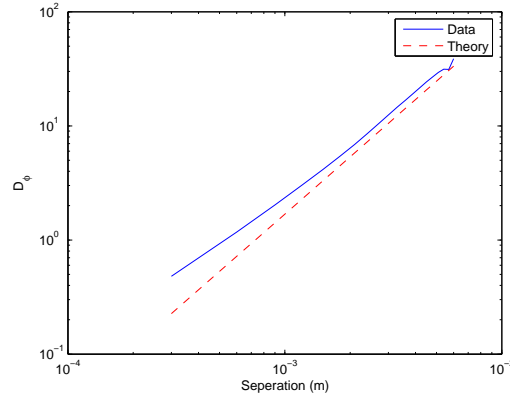Figure 4.21:   Scenario 1 Phase Structure Function.

Figure 4.22:   Scenario 2 Phase Structure Function.

4.5.3   Structure Function Evaluation.   Diffraction from the small square aperture of the SLM caused very large errors in the phase structure function of the experimental output. Diffractive phase errors cause the value of the structure function at low separations to be higher than expected. Also the diffractive intensity pattern causes the wavefront sensor to throw away data points or improperly measure others. Error was not quantified due to lack of faith in the results; however, it can be seen that the structure function still approximates a $\frac{5}{3}$ power law. Due to the error induced by diffraction section 4.5.4 is devoted to it entirely.
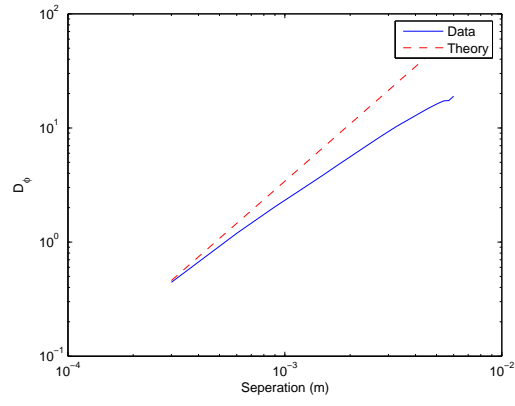
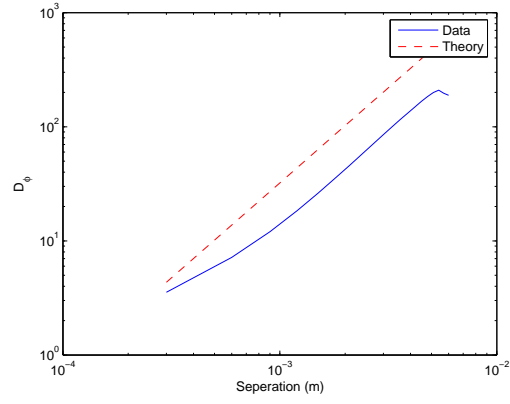Figure 4.23:   Scenario 3 Phase Structure Function.

Figure 4.24:   Scenario 4 Phase Structure Function.
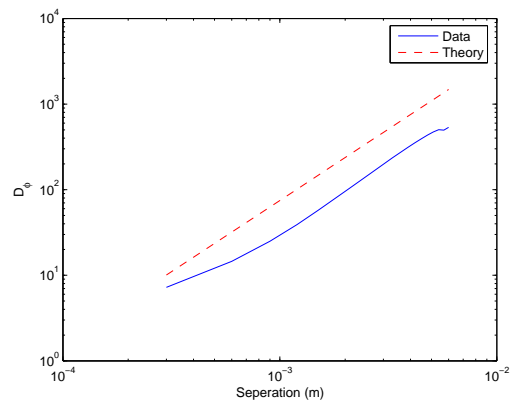

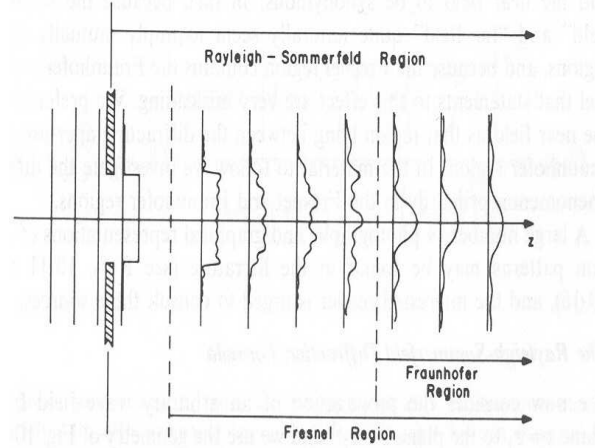Figure 4.25:   Scenario 5 Phase Structure Function.

Figure 4.26:   Changing diffraction pattern observed as a plane wave propagates through an aperture [6].

4.5.4   Diffraction.   It is a well know fact that diffractive effects are more pronounced for small Fresnel number propagation, that is when the aperture is very small or the path length is very large; this is shown graphically in Figure 4.26. The scenarios under test have Fresnel numbers on the order of 50 for the propagation between screens and 1000 for the last propagation. This means that diffraction is a problem for both propagations but is much more pronounced for the first propagation. Since the first propagation is so severely diffracted, then goes through a second aperture and is further diffracted the data is severely degraded. It should also be clear that this affects both amplitude and phase of the propagating field. Figures 4.27 - 4.32 show images taken at different points in the beam path; it is evident that the diffractive effects get worse with longer propagation. By having two small apertures in series with one another diffraction is further compounded. Also one can see a bright fringe around some of the images; this results from scattering off the edges of the SLM cover glass and the recess of the SLM housing.
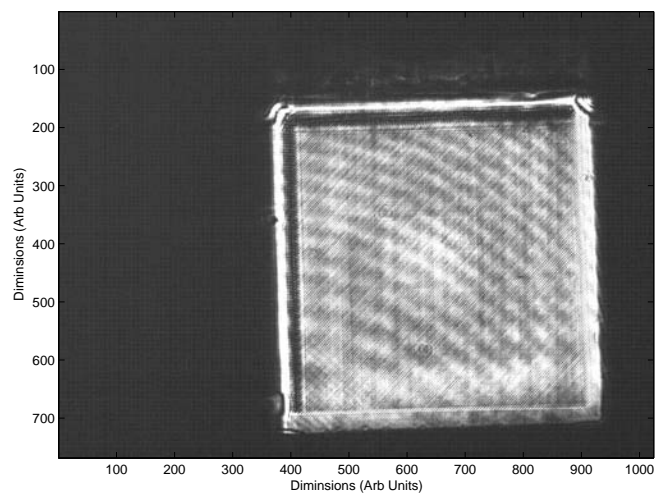
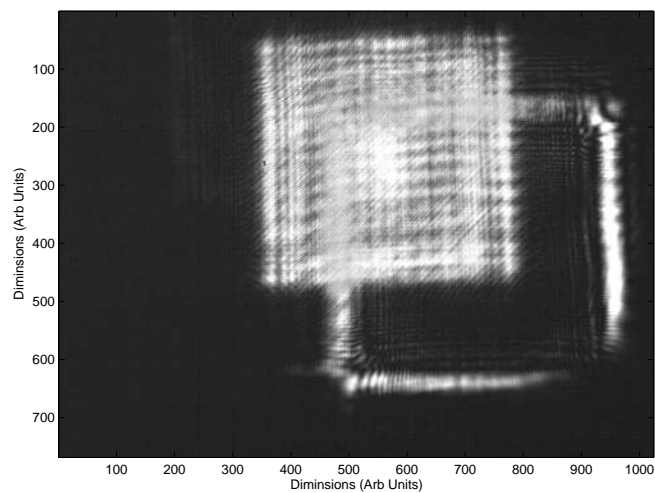Figure 4.27:   Image of plane wave 2 cm after second SLM.

Figure 4.28:   Image of plane wave 50 cm after second SLM.Note the square of non-steered energy resulting from scatter off of the SLM housing
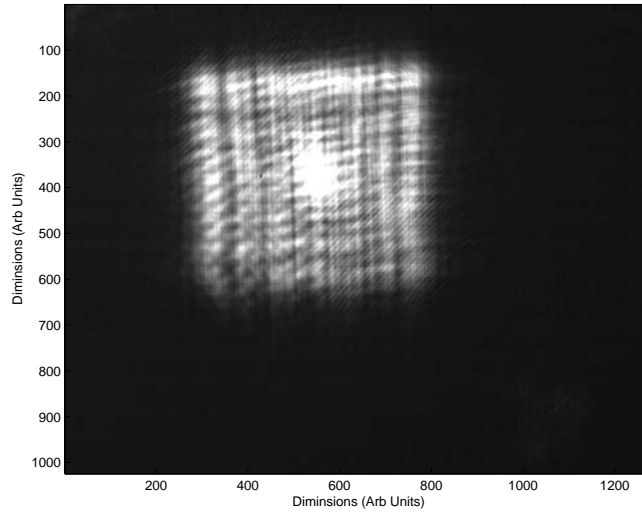
59

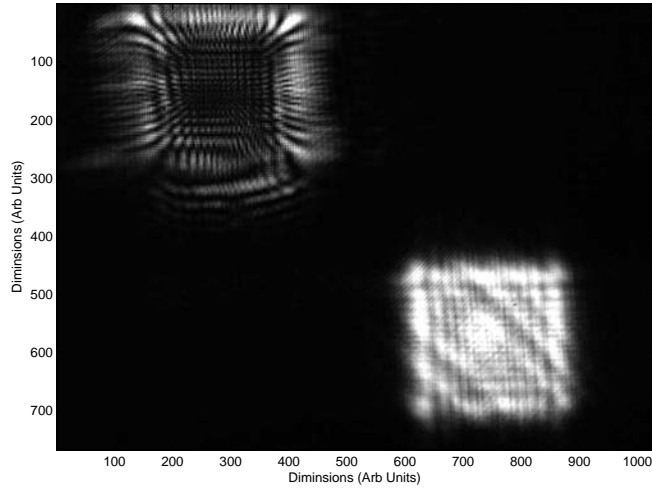Figure 4.29:   Image of plane wave 165 cm after second SLM.

Figure 4.30:   Reflection from first SLM with 95 waves of tilt in x and y. Steered beam is in lower left and zero order spot is in the upper left.
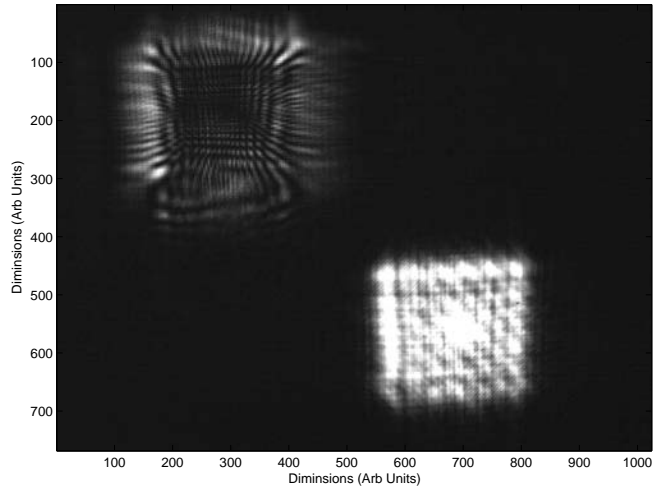
Figure 4.31: Reflection from second SLM with 95 waves of tilt in x and y. Steered beam is in lower left and zero order spot is in the upper left.
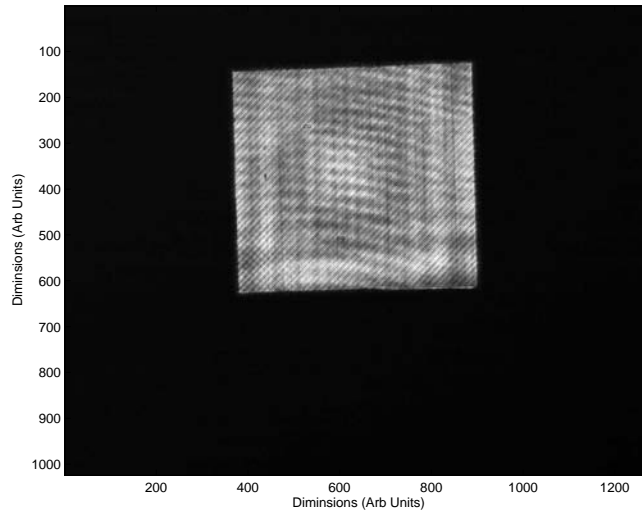

Figure 4.32: Reflection from second SLM with the edges masked to eliminate scattering from the SLM housing.
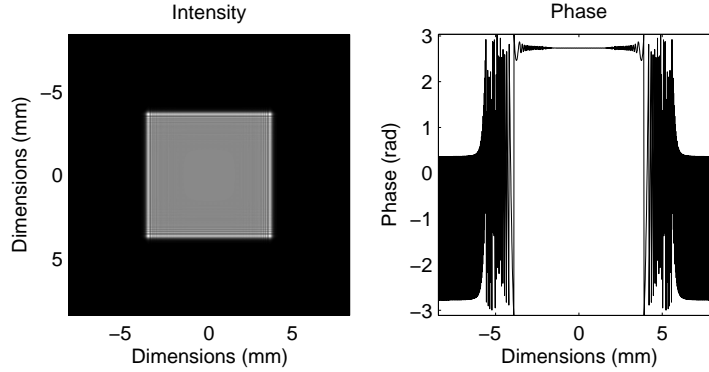
61

Figure 4.33:   Diffraction pattern 10cm after 7.68mm square aperture. Note that the wild phase variations are due to aliasing and has no impact since it is outside the region of interest.

4.6   Square Aperture Diffraction Simulations Results

Due to the tremendous data degradation from diffraction that was experienced in this research, these effects were isolated in a simulation. The simulation is written in Matlab. The simulation propagates an apodized plane wave using the Fresnel propagation integral. The simulation is performed for a single square aperture and data collected at $10cm$, $50cm$, $1m$, $2m$, and $3m$ beyond the aperture. The simulation was then reaccomplished with two apertures separated by $2m$ and data was collected at the same planes as above (beyond the last aperture). Figures 4.33 - 4.37 show the results of a single aperture; Figures 4.38- 4.42 show the results of two apertures. It can be clearly seen that the intensity and phase patterns resulting from diffraction get worse with longer propagation distances. This is no surprise; what is important to notice is how rapidly the pattern degrades as the beam goes through a second aperture. Reference [4] is similar research that did not see such severe diffraction effects, due to only using one SLM.
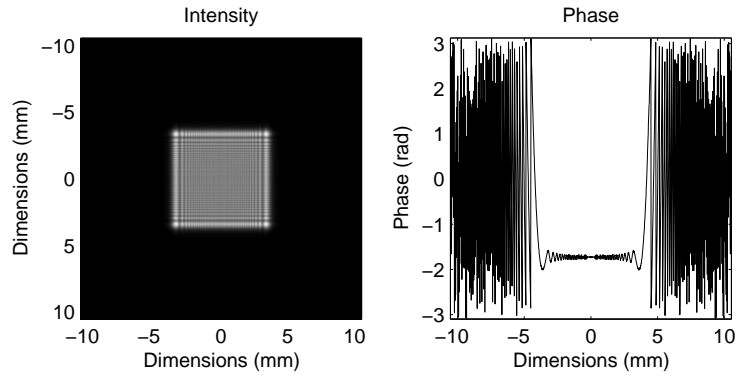
Figure 4.34:   Diffraction pattern 50cm after 7.68mm square aperture. Note that the wild phase variations are due to aliasing and has no impact since it is outside the region of interest.

Figure 4.35:   Diffraction pattern 1m after 7.68mm square aperture. Note that the wild phase variations are due to aliasing and has no impact since it is outside the region of interest.

Figure 4.36: Diffraction pattern 2m after 7.68mm square aperture. Note that the wild phase variations are due to aliasing and has no impact since it is outside the region of interest.

Figure 4.37: Diffraction pattern 3m after 7.68mm square aperture. Note that the wild phase variations are due to aliasing and has no impact since it is outside the region of interest.

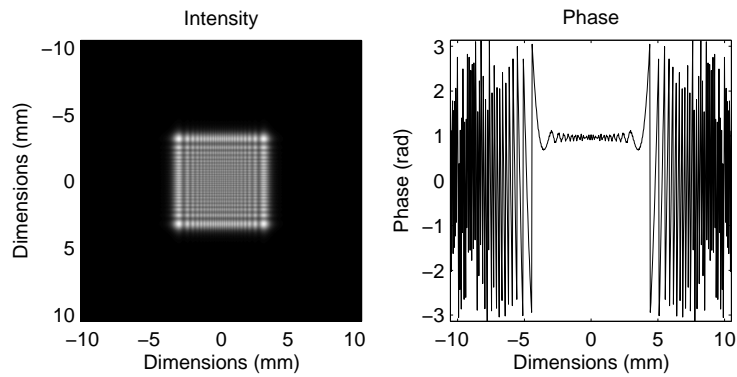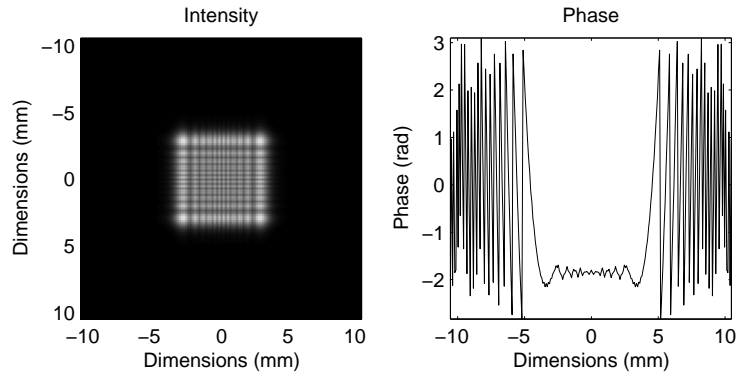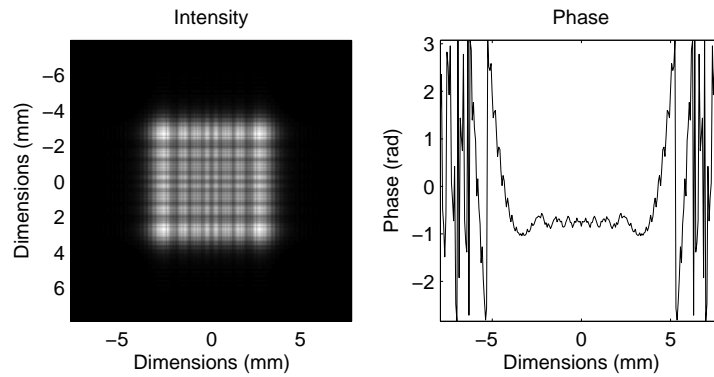Figure 4.38:   Diffraction pattern from two sequential 7.68mm square apertures. Apertures are 2m apart data collected 10cm from last aperture. Note that the wild phase variations are due to aliasing and has no impact since it is outside the region of interest.
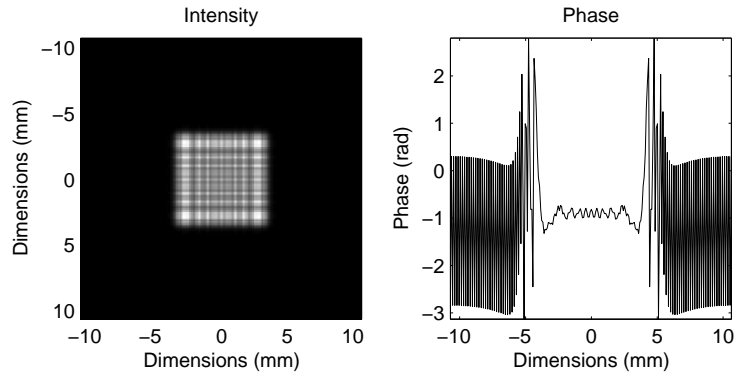
Figure 4.39:   Diffraction pattern from two sequential 7.68mm square apertures. Apertures are 2m apart data collected 50cm from last aperture. Note that the wild phase variations are due to aliasing and has no impact since it is outside the region of interest.
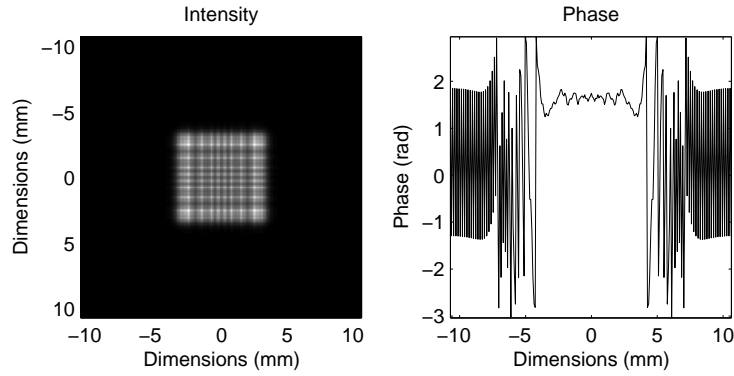
Figure 4.40:   Diffraction pattern from two sequential 7.68mm square apertures. Apertures are 2m apart data collected 1m from last aperture. Note that the wild phase variations are due to aliasing and has no impact since it is outside the region of interest.

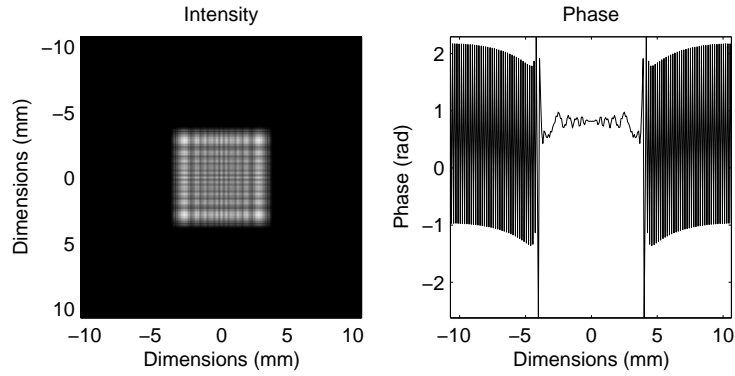

Figure 4.41:   Diffraction pattern from two sequential 7.68mm square apertures. Apertures are 2m apart data collected 2m from last aperture. Note that the wild phase variations are due to aliasing and has no impact since it is outside the region of interest.
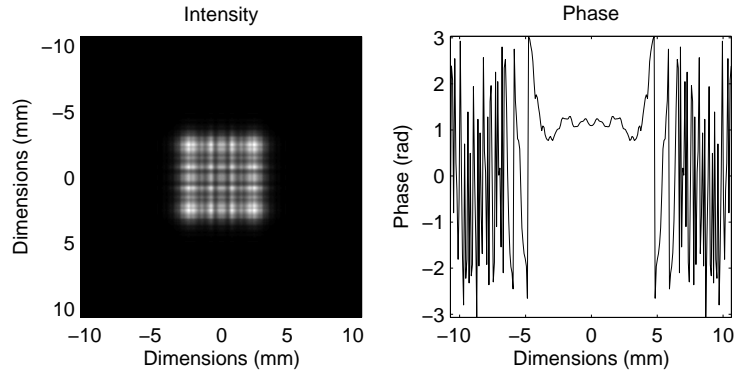
Figure 4.42: Diffraction pattern from two sequential 7.68mm square apertures. Apertures are 2m apart data collected 3m from last aperture. Note that the wild phase variations are due to aliasing and has no impact since it is outside the region of interest.
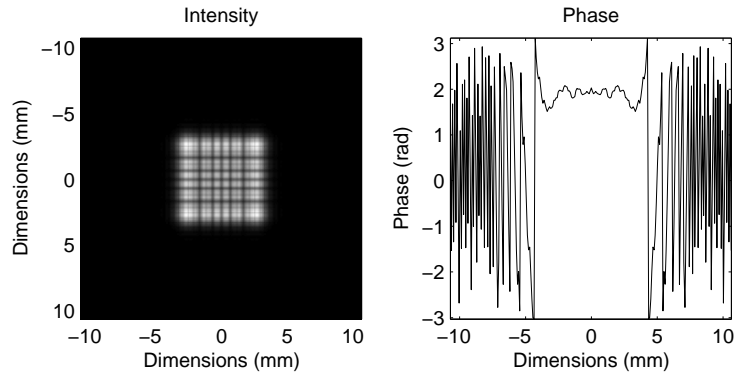
4.7 Summary

Data was collected over five turbulence cases; the data was then processed to give an intensity PDF and a phase structure function. From the processed data it could be determined how well the SLM system was able to model atmospheric turbulence. Diffraction was determined to be detrimental to the accuracy of phase data that was collected, while camera inadequacies and systematic error contributed to error in intensity data. Both phase and intensity data at least roughly followed the theoretical shape, which shows promise if these other effects can be mitigated.

V. Conclusions

5.1 *Introduction*

This research set out to design a system to mimic optical turbulence in the atmosphere in a laboratory environment. Motivation for this springs from the fact that laser systems are finding a home in many military applications; these applications include Space Situational Awareness (SSA), imaging and weapons systems.

The system used in this research used a phase only spatial light modulator from Boulder Nonlinear Systems to imprint phase abberations onto a wavefront. Two SLMs were placed in sequence in order to be able to control multiple atmospheric parameters independently. Data was collected in the lab and compared to theory and simulation.

5.2 *Research Results*

For this research five scenarios were examined. Each scenario is near identical in its geometry but with varying turbulence strengths. Case 1 is a nominal turbulence case ($r_0 = 6.9cm$ and $\sigma_1^2 = 0.179$). Cases 2 and 3 represent weaker turbulence cases while cases 4 and 5 are stronger. Simulation and experimental data was collected for each case.

5.2.1 Simulation results. The output of these simulations was processed to yield intensity PDFs and a phase structure functions for each scenario. Simulation yielded acceptable results with intensity PDF errors falling between 25% and 44% while phase structure function errors fall between 0% (within measurement precision) and 36%. Realizing that the errors may seem rather large, the simulations yielded PDFs and structure functions that had the proper shape. The errors can be attributed to the manner in which the Wavetrain software creates phase screens.

The analytical Rytov variance is higher than the measured for every case. This means that the simulation turbulence is, in a sense, weaker than expected. When Wavetrain creates phase screens the spatial frequency is linearly sampled; this

will under-represent the tilt variance, therefore under representing total turbulence strength. This under representation is seen as a lower Rytov variance.

For the structure functions a trend of note is that for weaker turbulence (cases 2 and 3) r_0 is smaller than expected (stronger turbulence) while for very strong turbulence (cases 4 and 5) r_0 is larger than expected. It is unclear from these results what is causing this.

5.2.2 Experimental results.   The experiment was constructed to model a scaled version of the simulation. Results were promising but some areas will still need to be addressed.

The intensity PDFs created for the five scenarios had error values ranging from 2% to 75%. The nominal case (case 1) had an error of only 2%, but the weakest and the strongest turbulence case had errors of 75% and 44% respectively. It is no surprise that the extreme cases had worse results since they required the hardware to be driven to further extremes. Also recall that the phase delay for each SLM is non linear function that must be calibrated and any error in this calibration will cascade into the experimental results.

The structure function error from the experiment was not quantifiable due to diffraction causing the shape to deviate slightly from theory. However, all the structure functions created were seen to roughly follow the $\frac{5}{3}$ power law.

5.3 Recommendations for future work

The results achieved in the research show promise but were not ideal, meaning there is more work that can be done. Recommendations for future work are improvement to the computer simulation codes and eliminating diffractive effects from the small apertures.

The Wavetrain software is a very functional wave optics propagation code, but it does not represent the atmosphere very accurately due to non ideal sampling.

The software allows for input of user generated screens; it would be worthwhile to compare results of wavetrain versus user generated screens for identical geometries and atmospheric PSDs. If this achieves betters results then the wavetrain code could be upgraded.

There are four possible ways to minimize diffractive effects. One is to shorten the propagation distances. This is really not practical since it is necessary to scale the separations of the SLMs to match the phase screen separation in the atmospheric model. A second approach would be to use larger SLMs. With a larger SLM you would have to be able to handle many more pixels or accept larger pixel dimensions. Analysis would be necessary to determine an acceptable range of pixel size for given turbulence cases. A third approach would be to study the diffraction caused by the aperture and determine if one can add an interfering phase on the SLM to erase the diffractive phase error. This would require the SLM to have enough dynamic range to handle diffractive phase errors being added to the desired atmospheric phase error. The fourth, and probably best, method for eliminating diffractive effects would be to use a Gaussian beam and under fill the aperture. It is well known that the soft apodization from a Gaussian beam will minimize diffractive effects. To further support this idea one can recall that a optical propagation can be modeled as a Fourier transform; since the Fourier transform of a Gaussian remains a Gaussian one can deduce that the input and output fields would be similar.

Bibliography

1. Andrews, Larry C. and Ronald L. Phillips. *Laser Beam Propagation through Random Media.* SPIE Press, Bellingham, Washington, 1998.

2. Andrews, Larry C. and Ronald L. Phillips. *Laser Beam Scintillation with Applications.* SPIE Press, Bellingham, Washington, 2001.

3. Boulder Nonlinear Systems. *User Guide: XY Phase Series Spatial Light Modulators Revision 2.8*, 2004.

4. Brooks, Mathew. *Atmospheric Simulation Using a Liquid Crystal Wavefront Controlling Device.* Master's thesis, Air Force Institute of Technology, March 2004.

5. Coy, Steve. *How to choose mesh spacing and mesh dimensions for wave optics simulation.* Technical report, MZA, Albuquerque, NM, April 2003.

6. Gaskill, Jack D. *Linear Systems, Fourier Transforms and Optics.* Wiley, New York, 1978.

7. Goodman, Joseph W. *Statistical Optics.* Wiley, New York, 1985.

8. Goodman, Joseph W. *Fourier Optics.* McGraw Hill, Boston, 1996.

9. Magee, Eric. *Phase Screens for Long Time Series Wave Optics Simulations.* Technical report, Mission Research Corporation, Dayton, OH, May 2003.

10. Roberts, Phillip. *A Wave Optics Propagation Code.* Technical report, tOSC, Anaheim, CA, December 1986.

11. Roggeman, Michael C. and Byron M. Welsh. *Imageing Through Turbulence.* CRC Press, Boca Raton, Florida, 1996.

12. Yariv, Amnon and Pochi Yeh. *Optical Waves in Crystals.* Wiley Interscience, New York, 1984.

REPORT DOCUMENTATION PAGE

1. REPORT DATE *(DD–MM–YYYY)*	2. REPORT TYPE		3. DATES COVERED *(From — To)*
21–03–2005	Master's Thesis		Sept 2003 — Mar 2005

4. TITLE AND SUBTITLE

Atmospheric Turbulence Simulation Using
Liquid Crystal Spatial Light Modulators

5a. CONTRACT NUMBER

5b. GRANT NUMBER

5c. PROGRAM ELEMENT NUMBER

6. AUTHOR(S)

Phillips, James D, Capt, USAF

5d. PROJECT NUMBER

5e. TASK NUMBER

5f. WORK UNIT NUMBER

7. PERFORMING ORGANIZATION NAME(S) AND ADDRESS(ES)

Air Force Institute of Technology
Graduate School of Engineering and Management
2950 Hobson Way
WPAFB OH 45433-7765

8. PERFORMING ORGANIZATION REPORT NUMBER

AFIT/GEO/ENG/05-01

9. SPONSORING / MONITORING AGENCY NAME(S) AND ADDRESS(ES)

AFRL/DES
3550 Aberdeen Avenue S.E.
Kirtland AFB, NM 87117-5776

10. SPONSOR/MONITOR'S ACRONYM(S)

11. SPONSOR/MONITOR'S REPORT NUMBER(S)

12. DISTRIBUTION / AVAILABILITY STATEMENT

Approval for public release; distribution is unlimited.

13. SUPPLEMENTARY NOTES

14. ABSTRACT

Laser systems are finding a home in many military applications - such as Space Situational Awareness, imaging and weapons systems. With an increasing focus on programs that entail atmospheric propagations, there is a need for a cost effective method of performing proof-of-concept demonstrations. The use of one SLM (single phase screen) to model atmosphere has been investigated previously with promising results. However, some effects cannot be captured with a single SLM. This paper focuses on the addition of a second SLM and quantifying the results. Multiple screens will allow the user to independently control the Fried parameter, the isoplanatic angle, and Rytov Variance. The research is comprised of simulation and experiment. The simulation demonstrates the ability to accurately model atmospheric effects with two phase screens. Based on the simulation, a hardware implementation was tested in the lab. This thesis describes the experimental set-up and results based on measurement of phase and intensity of the propagated field. It was noted that while analytic results are replicated in simulation, similar results in the lab were difficult to achieve.

15. SUBJECT TERMS

Spatial Light Modulator, SSA, SLM, Rytov, Fried Pararmeter, turbulence

16. SECURITY CLASSIFICATION OF:			17. LIMITATION OF ABSTRACT	18. NUMBER OF PAGES	19a. NAME OF RESPONSIBLE PERSON
a. REPORT	b. ABSTRACT	c. THIS PAGE			Maj Matthew Goda
U	U	U	UU	85	**19b. TELEPHONE NUMBER** *(include area code)* (937) 255–3636, ext 4614